PASSIVE SIGNATURE ENHANCEMENT IN THE OPTICAL REGIME USING MULTI-SUPERIMPOSED PARALLEL GRATINGS

AMÉLIORATION DE LA SIGNATURE OPTIQUE PASSIVE À L'AIDE DE RÉSEAUX DE DIFFRACTION PARALLÈLES MULTI-SUPERPOSÉS

A Thesis Submitted to the Division of Graduate Studies
of the Royal Military College of Canada

by

Amanda Ales, BSc
Captain

In Partial Fulfillment of the Requirements for the Degree of
Master of Science in Physics

April, 2026

Acknowledgements

I would like to thank Dr. Ribal Georges Sabat for taking me on as a student and developing a research idea that aligned with my career interests and aspirations. Your positive encouragement and guidance was instrumental in keeping me on track, and I appreciate your trust in me.

I also want to acknowledge the assistance of the entire Sabat Research Group, and specifically Dr. Yazan Bdour for his unwavering emotional and technical support. Having a group of experts to lean on was invaluable to the success of this project, as it gave me the confidence to carry forward during difficult times. Thank you all for letting me pester you.

Finally, I want to thank my family and friends for their encouragement and belief in me to complete this monumental undertaking which at times felt insurmountable. I would not have survived these past two years without your love and support.

Abstract

Passive spectral enhancement and signature management are of increasing importance across several emerging domains such as photonics, remote sensing, and defence applications including asset tracking and stealth. As photonic nanofabrication technologies progress toward compact, tunable, and scalable devices, this work addresses a technological gap in broadband signature enhancement using metasurfaces, with the goal of selectively widening the reflection bandwidth in the optical regime. This was achieved through the creation of multi-superimposed parallel gratings (MSPGs) using two distinct fabrication approaches. In the first method, up to ten discrete reflection peaks were generated at specific values across a broad optical bandwidth range (590–860 nm) by systematically increasing the grating pitch among successive superimposed layers. The average absolute error between the target and measured reflection wavelengths was ∼1.35%, demonstrating the precision of this technique. This method notably achieved broadband resonant filtering through controlled spectral distribution. A second MSPG-enabled enhancement strategy known as the continuous method was then investigated, in which the spacing between adjacent target reflection wavelengths was incrementally reduced until the peaks converged. This method was slightly less precise, as a global redshift in the data resulted in an average absolute error of ∼3.72%. Contrary to the anticipated broadband merging, the converged modes produced narrowed composite peaks, demonstrating tunable narrowband filtering behavior. These results establish MSPGs as versatile optical devices capable of producing engineered spectral 'fingerprints' that enable both broadband and narrowband optical responses. As such, they offer a promising platform to advance applications in signature management, spectral enhancement, and tunable photonic filtering.

Résumé

L'amélioration spectrale passive et la gestion de signature revêtent une importance croissante dans plusieurs domaines émergents tels que la photonique, la télédétection et les applications de défense, notamment le suivi d'actifs et la furtivité. À mesure que les technologies de nanofabrication photonique évoluent vers des dispositifs compacts, accordables et évolutifs, ce travail comble une lacune technologique en matière d'amélioration de signature à large bande à l'aide de métasurfaces, dans le but d'élargir sélectivement la bande de réflexion dans le régime optique. Cela a été réalisé par la création de réseaux parallèles multi-superposés (MSPG) à l'aide de deux approches de fabrication distinctes. Dans la première méthode, jusqu'à dix pics de réflexion discrets ont été générés à des valeurs spécifiques sur une large plage spectrale optique (590–860 nm) en augmentant systématiquement le pas du réseau entre des couches successivement superposées. L'erreur absolue moyenne entre les longueurs d'onde de réflexion ciblées et mesurées était d'environ $\sim$1.35%, démontrant la précision de cette technique. Cette méthode a notamment permis d'obtenir un filtrage résonant à large bande grâce à une distribution spectrale contrôlée. Une seconde stratégie d'amélioration basée sur les MSPG, appelée méthode continue, a ensuite été étudiée, dans laquelle l'espacement entre les longueurs d'onde de réflexion cibles adjacentes a été progressivement réduit jusqu'à ce que les pics convergent. Cette méthode s'est révélée légèrement moins précise, car un décalage global vers le rouge a entraîné une erreur absolue moyenne d'environ $\sim$3.72%. Contrairement à la fusion large bande anticipée, les modes convergés ont produit des pics composites plus étroits, démontrant un comportement de filtrage à bande étroite accordable. Ces résultats établissent les MSPG comme des dispositifs optiques polyvalents capables de produire des « empreintes spectrales » conçues, permettant des réponses optiques à large bande et à bande étroite. À ce titre, ils offrent une plateforme prometteuse pour faire progresser les applications en gestion de signature, en amélioration spectrale et en filtrage photonique accordable.

Contents

List of Tables

List of Figures

List of Acronyms

AFM	Atomic Force Microscope
DMS	Dielectric Metasurface
ECM	Extracellular Matrix
EM	Electromagnetic
FFT	Fast Fourier Transform
LiDAR	Light Detection and Ranging
LIL	Laser Interference Lithography
MSPG	Multi-Superimposed Parallel Grating
NDF	Neutral Density Filter
PS	Parallel-Superimposed
RPM	Revolutions Per Minute
SPR	Surface Plasmon Resonance
SPRi	Surface Plasmon Resonance Imaging
SRG	Surface Relief Grating
ViDAR	Visible Detection and Ranging

List of Symbols

Lower Case Symbols

Symbol	Description	Units (SI)
c	Speed of light in a vacuum	$\mathrm{m{\cdot}s^{-1}}$
k	Wave number ($k = \frac{2\pi}{\lambda}$)	$\mathrm{rad{\cdot}m^{-1}}$
k_0	Free space wave number	$\mathrm{rad{\cdot}m^{-1}}$
k_x	Tangential wave vector component	$\mathrm{rad{\cdot}m^{-1}}$
m	Diffraction order ($m = 0, \pm1, \pm2, \ldots$)	–
n	Refractive index	–
n_{eff}	Effective refractive index of the guided mode	–
n_{azo}	Refractive index of azobenzene thin film (core)	–
$n_{\mathrm{substrate}}$	Refractive index of substrate (cladding)	–
n_{air}	Refractive index of air (cladding)	–
t	Time	s
v	Phase velocity	$\mathrm{m{\cdot}s^{-1}}$
x, y, z	Cartesian spatial coordinates	m

Upper Case Symbols

Symbol	Description	Units (SI)
$B_{\mathrm{norm}}(\lambda)$	Estimated baseline of normalized reflectance spectrum (median filter)	–
$\mathbf{E}$	Electric field vector	$\mathrm{V{\cdot}m^{-1}}$
E_0	Amplitude of electric field vector	$\mathrm{V{\cdot}m^{-1}}$
$\mathrm{Err}_{\mathrm{abs}}$	Absolute wavelength error between target and measured resonances	%
$\mathrm{Err}_{\mathrm{spacing}}$	Absolute spacing error between adjacent resonance wavelengths	m
$\mathbf{H}$	Magnetic field vector	$\mathrm{A{\cdot}m^{-1}}$
H_0	Amplitude of magnetic field vector	$\mathrm{A{\cdot}m^{-1}}$
I	Irradiance	$\mathrm{W{\cdot}m^{-2}}$
$\mathbf{J}$	Current density	$\mathrm{A{\cdot}m^{-2}}$
K	Grating vector magnitude ($K = \frac{2\pi}{\Lambda}$)	$\mathrm{rad{\cdot}m^{-1}}$
K_n	Grating vector of the nth superimposed grating	$\mathrm{rad{\cdot}m^{-1}}$

Continued on next page

Symbol	Description	Units (SI)
N	Grating number ($N = 1, 2, 3$, etc.)	–
$R(\lambda)$	Raw measured reflectance spectrum as a function of wavelength	–
$R_{\text{corr}}(\lambda)$	Baseline corrected reflectance spectrum	–
$R_{\text{final}}(\lambda)$	Final normalized reflectance spectrum after baseline correction	–
$R_{\text{norm}}(\lambda)$	Normalized reflectance spectrum (min–max scaled)	–
$R_{\text{shift}}(\lambda)$	Reflectance spectrum after offset shift for visualization	–

Greek Symbols

Symbol	Description	Units (SI)
β	Propagation constant	$\text{rad}\cdot\text{m}^{-1}$
δ	Offset parameter to shift spectra above baseline	–
Δ	Separation distance	m
ϵ	Permittivity of a medium	$\text{F}\cdot\text{m}^{-1}$
ϵ_0	Permittivity of free space	$\text{F}\cdot\text{m}^{-1}$
ϵ_r	Relative permittivity	–
η	Wave impedance of a medium	Ω
η_0	Free space wave impedance ($\approx 377\,\Omega$)	Ω
λ	Wavelength	m
λ_m	Measured resonance wavelength	m
λ_t	Target resonance wavelength	m
μ	Magnetic permeability	$\text{H}\cdot\text{m}^{-1}$
μ_0	Permeability of free space	$\text{H}\cdot\text{m}^{-1}$
μ_r	Relative permeability	–
ρ_f	Free volume charge density	$\text{C}\cdot\text{m}^{-3}$
ω	Angular frequency	$\text{rad}\cdot\text{s}^{-1}$
θ	General angle	deg or rad
θ_i	Angle of incidence	deg or rad
θ_m	Diffraction angle	deg or rad
Λ	Grating pitch	m

Subscripts and Superscripts

Symbol	Description	Units (SI)
0	Denotes free space quantity (e.g. k_0, η_0, μ_0, ϵ_0)	–
i	Incident quantity (e.g. θ_i)	–
m	Diffracted quantity (e.g. θ_m)	–
m	Measured quantity (e.g., λ_m)	–

Continued on next page

Symbol	Description	Units (SI)
n	Grating index (e.g. Λ_n, K_n)	–
t	Target quantity (e.g., λ_t)	–
T	Total (e.g. Δ_T)	–

Chapter 1

Introduction

The experimental research presented in this thesis utilizes diffraction gratings as an optical waveguide mechanism to manipulate incident light, thereby widening the reflection bandwidth in the optical regime from a wavelength range of approximately 590 to 860 nanometers (nm). To contextualize diffraction gratings to the methodology and desired outcome of the research, this chapter introduces the concept by discussing the early history, principles, and types of diffraction gratings. Next, the interference lithography grating fabrication technique is discussed along with azobenzene and its relevant properties such as photoisomerization. A literature review of diffraction gratings in waveguide optics is then presented, focusing on applications such as signature enhancement via light coupling, filtering, and retroreflection. Gaps in the literature are then discussed before transitioning into the goal of the research and document outline.

1.1 Brief Introduction to Diffraction Gratings

1.1.1 Early History of Diffraction Gratings

The concept of diffraction gratings dates back to the 17th century, when Scottish mathematician and astronomer James Gregory made the first recorded observation of a naturally occurring diffraction grating in 1673 [1]. He passed sunlight into a dark house through a small hole, placed a white bird feather in front of it and observed the beam of light split into various circles and colours against a white wall. He also noted the near-equal size and spacing of the branches or barbs that extended from the feather shaft, an important property that is required for diffraction to occur [1]. Over a century later in 1785, the first recorded human-made diffraction grating is widely accepted to have been created by American inventor David Rittenhouse [2]. Rittenhouse created a square of approximately 50-60 hairs, each one parallel and equidistant from one another and vertically strung between two finely cut screws [3]. He then placed them in front of a vertical slit carved into a window shutter. Upon shining sunlight through the slit in a dark room, he noticed the formation of parallel lines that decreased in intensity the further they strayed from the centre beam. In 1821, German physicist Joseph von Fraunhofer independently produced similar experiments to Rittenhouse by winding threads and wires around screws [3, 4]. However, due to von Fraunhofer's advanced understanding and innovation in the field of diffraction, including the derivation of the grating equation and using gratings to obtain line spectra, he is accredited for pioneering the use of gratings in spectroscopic analysis.

1.1.2 Principles of Diffraction Gratings

A diffraction grating can be defined as any arrangement of optical elements that periodically modulate one or more properties of an incident electromagnetic (EM) wave, such as its electric field amplitude, phase, or both [5, 6]. The optical elements are separated by a distance d, also known as the grating pitch Λ, the magnitude of which must be comparable to the wavelength of the incident light in order for diffraction to occur. Figure 1.1 illustrates the diffraction of light in reflection and transmission, highlighting the rays' direction of travel before and after interacting with a plane grating. The theory section will further expand upon this concept at a fundamental level, explaining other additional factors that impact the light propagation or dispersion. For example, how the incident angle (shown as α in the below diagram) relates to the diffracted angles (represented by β).

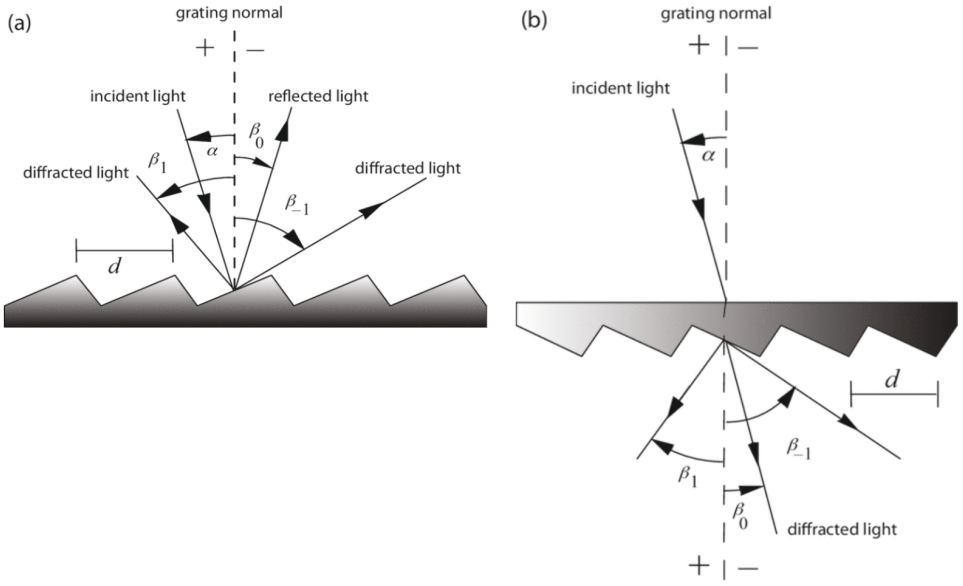

Figure 1.1 – Light ray propagation upon interaction with a plane wave diffraction grating in a) reflection and b) transmission [6].

When an incident electromagnetic wave is reflected from or transmitted through a diffraction grating, it is dispersed into multiple beams known as diffraction orders. This phenomenon occurs due to the principle of interference, as the periodic grating structure disperses the light depending on the grating type. When light waves reflect off of or transmit through periodic grating elements, they are scattered by successive grating periods and interfere with one another [6]. At specific angles, the waves that are in phase with one another will combine to produce constructive interference, known as diffraction maxima. These intensity maxima are characterized by integers known as diffraction orders ($m = 0, \pm 1, \pm 2, \dots$). Conversely, the waves that are out of phase at specific angles will cancel each other out resulting in destructive interference, known as diffraction minima. This concept is depicted for a plane wave in Figure 1.2.

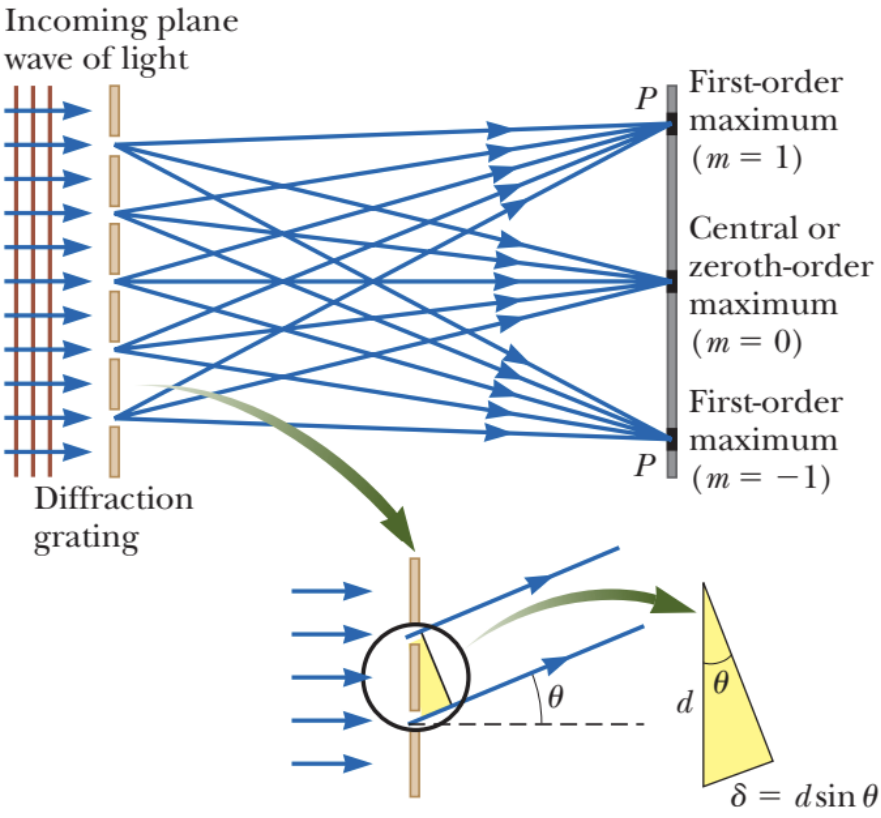

Figure 1.2 – Schematic of constructive interference as a result of light interacting with a plane wave diffraction grating [7].

1.1.3 Types of Diffraction Gratings

There are many different grating types that can be used for a wide range of scientific applications. The two broadest categories are reflection and transmission gratings which are classified by light interaction based on the properties of the grating material, that is, whether diffraction occurs from or through the grating surface [8]. As mentioned earlier, gratings may also be categorized by their ability to periodically modulate an EM wave's amplitude, phase or both. Amplitude gratings spatially modulate the optical intensity of incident waves by periodically varying the reflection, transmission, or absorption. This results in a change in amplitude of the diffracted waves in both reflection and transmission gratings [9]. By contrast, phase gratings periodically vary the shape of an emerging wavefront by altering its optical path length through variations in refractive index or surface relief. In addition to amplitude gratings, phase gratings can also apply to both reflection and transmission gratings.

These grating types can be further divided into ruled and holographic gratings as shown in Figure 1.3, which are classified by their manufacturing method and resulting grating profiles [8]. Ruled gratings are fabricated by mechanically inscribing grooves in the substrate using tools such as diamond cutters and ruling engines. This method is tedious and requires extreme precision, however it is useful for obtaining triangular or sawtooth grating profiles as depicted in Figure 1.3(a). These profiles enhance diffraction efficiency as the grooves are optimized to concentrate diffracted

light into a specific diffraction order. In holographic gratings, grooves can be inscribed through photographic recording or lithography by exposing a photographic plate to an interference fringe field [6, 10]. This technique generally results in a sinusoidal profile as shown in Figure 1.3(b), and it can be used to create surface relief gratings (SRGs) which are the grating type investigated in this thesis.

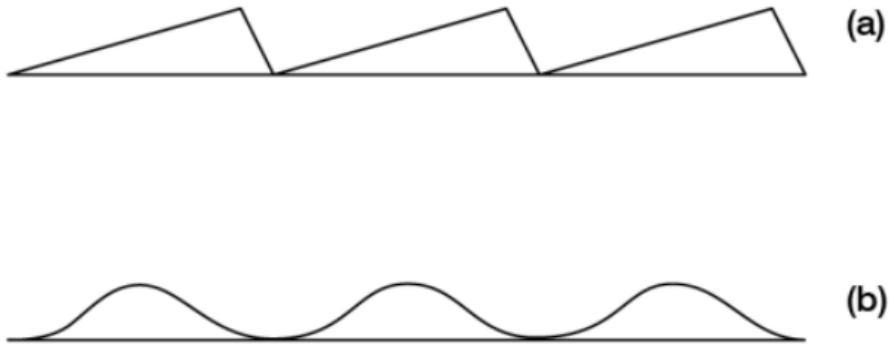

Figure 1.3 – Ideal grating profiles for ruled (a) and holographic (b) gratings [6].

1.2 Interference Lithography and Photoisomerization

This subsection further expands upon interference lithography by contextualizing it with the research conducted in Chapter 4. In interference lithography, a photomechanical material can be deposited on a photographic plate and exposed to an interference pattern which is then imprinted onto the sample. In this research, a laser interference lithography (LIL) technique was used to create an interference pattern by intersecting two sets of monochromatic single-beam laser waves. To ensure the pattern is precise, these waves must be coherent and identical in intensity, polarity, and wavelength [6]. The LIL technique typically creates a sinusoidal grating profile as shown in Figure 1.3(b), and can thus be used to create SRGs which were employed in the research for this thesis.

To further understand LIL, it is important to discuss the photomechanical process. Photomechanical materials are light-sensitive, meaning their chemical or physical properties can be altered in the presence of light which can be exploited through LIL to create a desired interference pattern. A photomechanical material of particular relevance to this work is a class of chemical compounds known as azobenzene, which was shown in the 1990s to undergo trans-cis photoisomerization under optical illumination [11, 12]. This photoisomerization property of azobenzene-containing polymers elicits photoinduced molecular motion, in which isomers of azobenzene rapidly convert between their cis and trans forms upon exposure to polarized light such as that produced in LIL. Figure 1.4 illustrates this process [13]. Azobenzene is a particularly desirable photomechanical material in LIL SRG fabrication as it retains its optical properties after one or multiple parallel-superimposed inscriptions, including its ability to diffract and couple light.

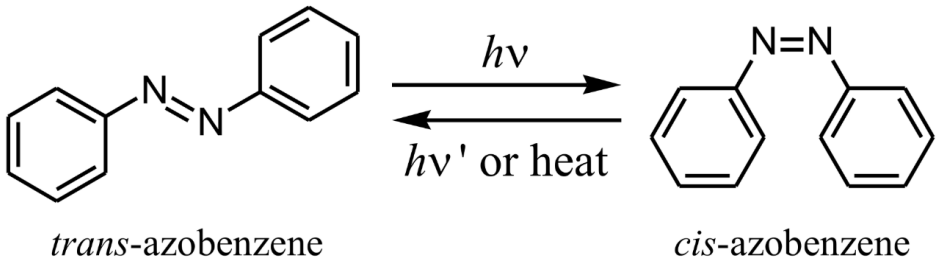

Figure 1.4 – Trans-cis photoisomerization of azobenzene-containing polymers upon exposure to polarized light [13].

1.3 Literature Review of Diffraction in Waveguide Optics

1.3.1 Diffraction Gratings in Spectroscopy

The diffraction grating is one of the most important inventions in modern science, specifically through its contribution to the field of spectroscopy. Gratings can be used to disperse polychromatic light into its monochromatic constituents, and the resulting emission and absorption spectra act as a unique fingerprint or identifier for the object being observed, be it an Earth-bound element or a distant galaxy [14]. This spectroscopic utility spans across every domain of the natural sciences, including physics, chemistry, and biology, and these interdisciplinary applications are ever-expanding. Gratings can be used to observe and analyze electromagnetic spectra and their interactions from the subatomic to macrophysical level, and they have led to some of the most significant discoveries of the past quarter millennium. For instance, diffraction gratings were instrumental in determining the structural composition of the hydrogen atom, which verified key theories and made new discoveries in the fields of quantum physics and cosmology. It allowed scientists to predict with confidence the age and expansion of our universe through analyzing the chemical composition, temperature and movement of astronomical objects. Given the vast range of applications for diffraction gratings, this section narrows the scope to the context of the research. A literature review of spectroscopic applications of diffraction gratings is conducted, specifically focusing on waveguide optics, metasurfaces and signature enhancement.

1.3.2 Waveguide Optics and Diffraction Gratings

One of the most common applications of diffraction gratings is their use as an optical waveguide. An optical waveguide can be defined as a physical structure that guides the movement of light waves in the optical portion of the EM spectrum. This structure consists of a core (usually hollow) surrounded by a cladding or substrate that confines light [15]. The refractive index of the cladding must be lower than that of the core, and this differential allows light to be contained to the waveguide as it sets the conditions for total internal reflection to occur.

Optical waveguides can be classified by a range of categories. Geometric shape is one, with some examples including planar or dielectric (slab) waveguides, rectangular, cylindrical (channel), or fibre optic configurations. For reference, Figure 1.5 illustrates a slab and channel waveguide. Other categories include the waveguide's composite material, mode propagation, and distribution of refractive index [16]. These factors collectively determine a myriad of important properties, including but not limited to: the direction or confinement of wave propagation, the dimension(s) of propagation (1D, 2D, 3D), the range of frequencies that may propagate, and the modes or EM field

distribution patterns that satisfy the phase-matching condition (i.e. transverse electric, transverse magnetic, etc). These properties help narrow the application that a specific waveguide may be used for. Chapter 2 will delve further into the theory of optical waveguides.

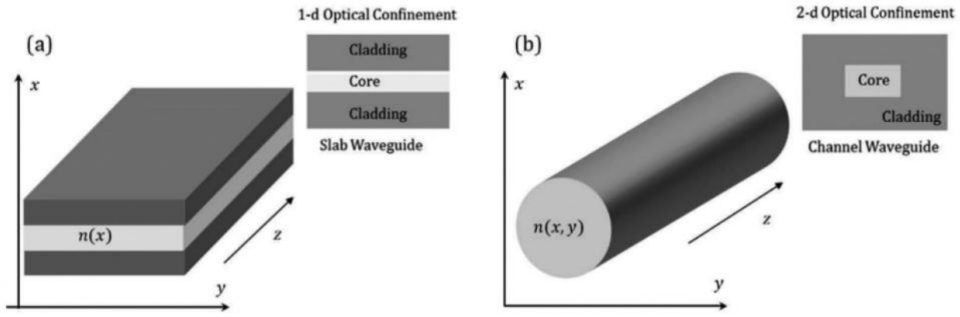

Figure 1.5 – Waveguide configurations for slab (a) and channel (b) optical confinement [16].

While there are many types of optical waveguides, this section focuses on waveguide diffraction gratings and their effects on signature enhancement according to the literature. Waveguide diffraction gratings employ periodic modulations in surface relief or refractive index to diffract, couple, and sometimes retroreflect light, thereby enabling spectral filtering. As previously mentioned, the research presented in this thesis consists of azobenzene-coated SRGs fabricated via LIL. The light diffracted from these SRGs can be modeled using the dielectric planar (slab) waveguide structure. The azobenzene thin film layer serves as the waveguide core, with two layers of cladding including the surrounding glass substrate and air. The resulting contrast in refractive index enables one dimensional transverse optical confinement in the x direction, while light propagates along the longitudinal z direction. The thin film supports grating coupling as its surface undergoes periodic modulation due to photoisomerization, which enables SRG formation through photoinduced mass transport of the azobenzene molecules. In this case, the SRG itself serves as the coupler or coupling mechanism [17].

1.3.3 Applications of Metasurfaces

It is important to note that the SRGs employed in this thesis are not only waveguide diffraction gratings, but can also be classified as a type of metasurface. Metasurfaces can be defined as resonant, thin optical elements that are composed of smaller, sub-wavelength nanostructures known as meta-elements arranged in a 2D plane [18]. These meta-elements influence various EM field properties surrounding the metasurface interface including phase, amplitude, and polarization, which affect wave propagation and scattering [19]. The thinness of these metasurfaces are a desirable evolution compared to conventional optical equipment as they are several orders of magnitude smaller than the typical components which are relatively large and bulky [20]. They can be grouped into two main categories based on their composite material: metallic and dielectric metasurfaces (DMSs). Metallic metasurfaces are coated in a metal such as silver or gold and take advantage of surface plasmon resonance (SPR) oscillations, while DMSs utilize dielectric materials to induce surface resonance. As discussed in Chapter 1.2, a prominent dielectric material used in LIL-fabricated SRGs is azobenzene as it confines the light by introducing a high refractive index differential between itself (the thin film) and the glass substrate. This supports SRG formation through the aforementioned process of photoinduced molecular motion or photoisomerization.

Metasurfaces have a vast set of capabilities and interdisciplinary applications, and their relevance to this work will be addressed. At an overarching level, they are highly useful in the optics domain as they can act as surface waveguides for light. Metasurfaces also provide surface impedance that can be specially modified to enable absorption, cloaking and stealth applications [21–23]. Additionally, metasurfaces can be used as antennae in optical communications as they enable beam formation and steering as well as leaky wave mode radiation, thereby enhancing antenna performance [24–26]. This type of radiation allows for tunability of the amplitude and phase of diffracted waves at a fixed frequency in both transmission and reflection modes.

Metallic metasurfaces guide and manipulate EM fields at the metal-dielectric interface through the excitement of collectively oscillating free electrons [27]. This facilitates surface plasmon resonance or SPR by coupling the incident waves into surface plasmon modes that match the necessary resonant conditions [28]. This effect results in a heightened optical response that is highly sensitive, which can be exploited for SPR imaging (SPRi). In addition to optics, SPR and SPRi are useful in many fields including nanophotonics, biomedicine, and biosensing [20, 29–31]. Figure 1.6 shows an SPRi composite image of an extracellular matrix (ECM), thus capturing the observation of live cell engagement in real time. The ability to image these processes contributes to the scientific understanding of the spread of diseases and cancers, and ultimately how to prevent them [32]. ECM SPRi is also useful for characterizing wound healing at a cellular level.

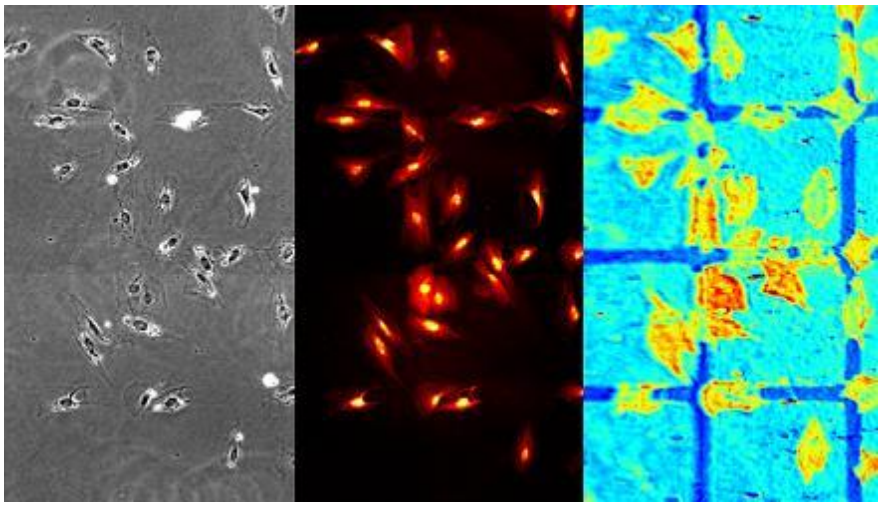

Figure 1.6 – SPRi composite image of an ECM to observe cell behaviour in real time, thus advancing understanding of diseases, cancers, and wound healing [32].

DMSs are also useful for enhanced imaging and sensing as a result of the surface resonance they induce, and this gives them some advantages over metallic metasurfaces. Their materials are lower cost, and they exhibit low Ohmic loss or low resistance in the visible regime, which translates to ultrahigh efficiency in transmission [19]. Another emerging application of DMSs is in the field of quantum optics. For example, DMSs are extremely useful for quantum state reconstruction and the miniaturization of quantum systems in order to conceptualize the spin and momentum of quantum particles [33, 34].

1.3.4 Coupling and Retroreflection

The previous subsections briefly introduced the ability of waveguide diffraction gratings to couple and retroreflect light as a means to enable spectral filtering, which is the overarching goal of this research. Fabricating DMS gratings using azobenzene is a proven method to enable and enhance the coupling process. Coupling occurs when light is guided into and out of a waveguide structure (in this case, grating) through the diffraction of the incident waves, as a result of their interaction with the holographic or LIL-fabricated sinusoidal structure that modulates periodically. When coupling takes place at a preselected angle of incidence or wavelength, the grating can function as an optical filter [12] which is useful in many of the aforementioned applications such as imaging, sensing, spectroscopy, and spectral management, the latter of which will be discussed in Chapter 1.3.5.

An additional developing application of gratings is their use as retroreflectors, which are optical devices that reflect incident light back in the direction of its source [35]. While basic geometric retroreflectors such as corner-cube and spherical configurations are well understood, there is a need to significantly scale down the size and modify the design to meet the evolving demands of today's optical systems, as they are becoming increasingly miniaturized and tunable. This has prompted the development of grating-based retroreflectors, a fast-growing area of research. In recent literature, these have been fabricated in a parallel-superimposed (PS) configuration with two gratings inscribed on top of one another, known as a bi-grating, to support coupling and SPR at a monochromatic target wavelength.

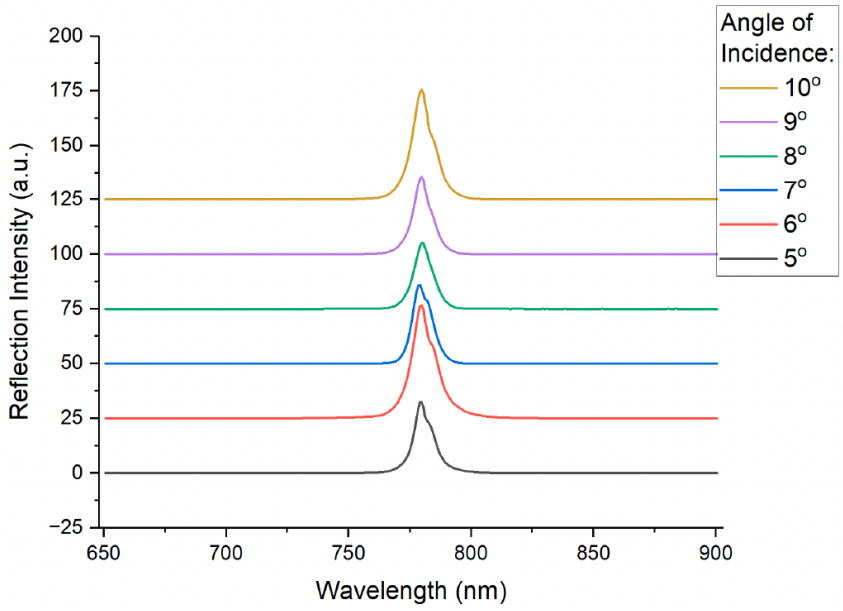

Figure 1.7 – Monochromatic retroreflection at a target wavelength of 785 nm depicted in 2D for six bi-grating samples at varying angles of incidence [35].

The azobenzene-coated SRGs produced in this research combine these coupling and retroreflection processes with the PS fabrication method to enable signal enhancement, a desirable outcome for this work. This study also explores the effects of inscribing multiple PS gratings, and pushes the boundary of how many gratings can be 'stacked' while maintaining a reasonable coupling efficiency, which translates to a clear and an enhanced spectral response.

1.3.5 Signature Management and Filtering

Another application of diffraction gratings in waveguide optics is for signature management, in which an object's spectral signature is intentionally modified to achieve a desired effect. This is a critical aspect of military operations as its relevance spans across all branches including land, sea, air and space. Signature management is important for stealth, remote sensing, and air and spacecraft optical asset tracking via LiDAR (Light Detection and Ranging) and ViDAR (Visible Detection and Ranging) as it can be used to reduce the possibility of detection while conducting operations. While a wide variety of signature management technology exists, the use of optical thin film coatings such as SRGs are a relevant and evolving option.

Since gratings can act as both filters and couplers of light, they can be used to modify spectral signatures by manipulating the incident light waves to enhance reflection or transmission [36]. Gratings can enable wavelength-selective coupling of a waveguide's guided modes or characteristic waves, which are imposed by the phase-matching condition or resonance which is directly tied to the grating pitch [15, 16]. This can be exploited for resonant or narrowband filtering, in which the spectrum of reflected or transmitted light is reduced as much as possible to create sharp peaks. Figure 1.8 depicts this concept and contrasts it against broadband filtering which is discussed in the following paragraphs [37].

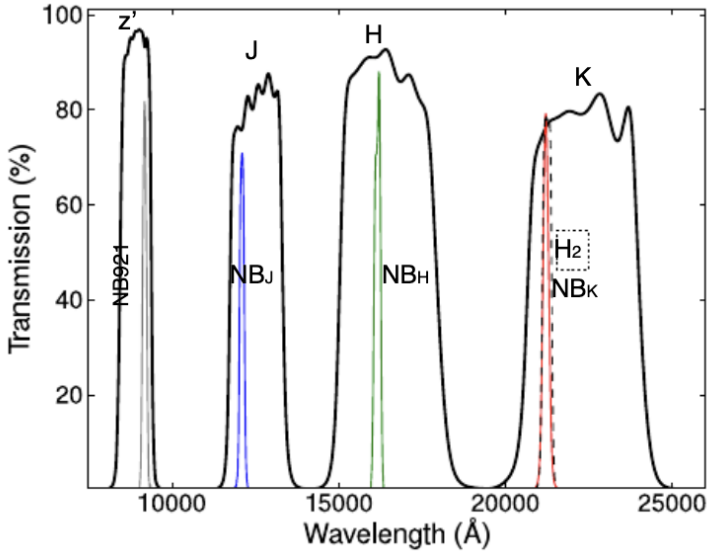

Figure 1.8 – Narrowband versus broadband filtering example for z, J, H, and K bands which identify stellar redshifting to determine the rate of star formation in galaxies [37].

This particular graphic applies to astrophysical spectroscopy in the context of star-forming galaxies, however the concept remains the same for filtering using diffraction grating waveguides. These waveguides are highly selective and highly sensitive, as the wavelength(s) of interest must match with that of the natural or fabricated resonance of the filtering structure in order for it to work. Plenty of research has been dedicated to this particular area of study, and this type of filtering has been demonstrated using azobenzene-coated SRGs [17] which is the basis of the work presented in this thesis. Conversely, waveguides can also be exploited for non resonant or broadband applications in which the spectrum of reflected light is expanded or widened. This can be achieved through the facilitation of absorption or scattering interactions, in which case the phase-matching

condition does not need to be met.

Although narrowband purposes are more common, some waveguide applications such as signature enhancement may require broadband technology. Widening the reflection or transmission bandwidth can have a camouflage effect in which an object blends into the spectroscopic background, thus avoiding optical detection by concealing its spectral signature. This area of research is emerging, and after extensive search it has been determined that the open source literature on this topic is limited - especially as it pertains to azobenzene-coated parallel-superimposed SRGs. Thus, this research aims to fill the gap of metasurface broadband spectral filtering in the optical regime. Notably, this work achieves a broadband effect using resonant filtering, an unlikely and underdeveloped combination.

1.4 Thesis Statement

The goal of this research is to achieve broadband signature enhancement in the optical regime by widening the reflection bandwidth via multi-superimposed parallel gratings (MSPGs) using systematic pitch variation. These azobenzene-coated MSPGs are a type of metasurface that were intentionally fabricated to generate as many spectral responses as possible over a widened reflection bandwidth.

This work is novel as the number of parallel-superimposed (PS) or stacked gratings within a single MSPG, denoted as N, ranged from $N = 1$ to $N = 10$. This exceeds the maximum number of PS gratings ever recorded in the literature, and this thesis investigates two separate methods by which this signature enhancement was achieved:

1) Discrete spectral enhancement, in which distinct reflection peaks ranging from $N = 1$ to $N = 10$ were evenly distributed across the 590-860 nm target wavelength bandwidth, resulting in the observation of up to ten discrete reflection peaks across a $\sim$270 nm range; and

2) Continuous spectral enhancement, in which each set of discrete reflection peaks for the $N = 2$ to $N = 10$ discrete MSPGs were progressively merged into one combined peak by incrementally decreasing the spectral spacing between adjacent resonances.

1.5 Thesis Structure

This thesis is divided into five chapters. Chapter 1 introduces several important concepts related to diffraction gratings, including a brief historical overview, fundamental principles, and common grating types, in order to contextualize the research presented in this work. An overview of interference lithography and photoisomerization is then provided, followed by a literature review of the applications of diffraction gratings in waveguide optics with an emphasis on filtering, coupling and retroreflection. The chapter concludes with the thesis statement and an outline of the document.

Chapter 2 delves into the EM theory of diffraction gratings, including relevant derivations. It reviews EM theory as it applies to waveguides, and covers a range of topics such as energy fields, the wave nature of light, Maxwell's equations, interference and diffraction grating theory, dispersion, and Fast Fourier Transform (FFT). The chapter further expands on the principles of signature enhancement via photon coupling and retroreflection in the context of waveguiding optics.

Chapter 3 outlines the experimental methods that were employed to validate the theoretical framework laid out in Chapter 2 and obtain the results presented in Chapter 4. It describes the complete experimental setup, from azobenzene thin film sample preparation, to the Lloyd's mirror interferometer, in which LIL is used to fabricate MSPGs. Next, this chapter details the two experimental methods used to widen the reflection bandwidth and achieve signature enhancement.

The reflection spectroscopy setup is also described, focusing on the process used to measure the samples' spectral responses in terms of reflectance versus wavelength reflection peaks. Finally, it presents the surface characterization and analysis methods that were used to extract the 1D FFT data for the spectral validation discussed in Chapter 4.

Chapter 4 presents the results of the experiments outlined in Chapter 3 and discusses the successes, limitations, and potential improvements. It also considers the broader impact of this research to the field of optics.

Chapter 5 summarizes the research and proposes avenues for future work to build upon the results achieved in this study.

Chapter 2

Theory

In order to understand the mechanism of light propagation in waveguide diffraction gratings, it is important to first provide a brief review of the fundamental properties of EM waves. This includes a comparison of wave propagation through various media, namely free space versus dielectric materials such as slab waveguides. Diffraction grating theory will then be explored, with a specific focus on EM wave interaction in multiple or 'stacked' PS gratings. The physics of waveguide optics, coupling, and retroreflection are then expanded upon to better understand the concept of signature enhancement in the context of this work. Finally, Fourier optics are introduced to describe the post-spectroscopic analysis conducted in the results section.

2.1 Electromagnetic Wave Propagation

2.1.1 Maxwell's Equations in Various Media

Throughout the nineteenth century, the scientific fields of electricity and magnetism made significant developments which forever altered the trajectory of modern physics and accelerated humanity's understanding of optics. These developments culminated in mathematician James Clerk Maxwell's revolutionary equations which combined these previously independent fields into what is now known as electromagnetism, as well as his postulation that light waves are indeed EM waves [5]. Maxwell's equations are undoubtedly some of the most important and fundamental mathematical models in physics, as they form the theoretical basis that govern the laws of all EM interactions. The differential form of Maxwell's equations for EM fields through a homogeneous, isotropic and linear dielectric medium are shown below. These are commonly referred to in order as: Gauss's law for electric fields, Gauss's law for magnetic fields, Faraday's law of induction, and Ampère's law [5, 9, 38, 39]:

$$\nabla \cdot \boldsymbol{E} = \frac{\rho_f}{\epsilon} \tag{2.1.1}$$

$$\nabla \cdot \boldsymbol{H} = 0 \tag{2.1.2}$$

$$\nabla \times \boldsymbol{E} = -\mu \frac{\partial \boldsymbol{H}}{\partial t} \tag{2.1.3}$$

$$\nabla \times \boldsymbol{H} = \boldsymbol{J}_f + \epsilon \frac{\partial \boldsymbol{E}}{\partial t} \tag{2.1.4}$$

In these equations, the electric vector field is represented by $\boldsymbol{E}$ and the magnetic vector field

intensity as $\boldsymbol{H}$. Although not present in the above equations, the magnetic flux density $\boldsymbol{B}$ is related to $\boldsymbol{H}$ through $\boldsymbol{B} = \mu\boldsymbol{H}$. The total free charge density is represented by ρ_f, and the free current density by $\boldsymbol{J}_f$. The permittivity is given by $\epsilon = \epsilon_0\epsilon_r$, where ϵ_0 is the permittivity of free space and ϵ_r is the relative permittivity of the medium. Similarly, the magnetic permeability is given by $\mu = \mu_0\mu_r$, where μ_0 is the magnetic permeability of free space and μ_r is the relative permeability of the medium. The work in this thesis only considers non-magnetic materials, so the permeability can be approximated to that of free space where $\mu_r \approx 1$ therefore $\mu = \mu_0$.

In free space or a vacuum void of charge and current, ρ_f and $\boldsymbol{J}_f$ reduce to zero, resulting in the following form of Maxwell's equations:

$$\nabla \cdot \boldsymbol{E} = 0 \tag{2.1.5}$$

$$\nabla \cdot \boldsymbol{H} = 0 \tag{2.1.6}$$

$$\nabla \times \boldsymbol{E} = -\mu_0 \frac{\partial \boldsymbol{H}}{\partial t} \tag{2.1.7}$$

$$\nabla \times \boldsymbol{H} = \epsilon_0 \frac{\partial \boldsymbol{E}}{\partial t} \tag{2.1.8}$$

2.1.2 Wave Characterization

EM waves are categorized as being transverse, meaning the direction of propagation is perpendicular to the direction of oscillation [5]. The EM field itself represents a state of excitation by the presence of electric charges, and it is made up of two vector components, the electric vector field $\boldsymbol{E}$ and magnetic vector field $\boldsymbol{H}$. These vector fields oscillate in two perpendicular planes, and can be illustrated by Figure 2.1 below.

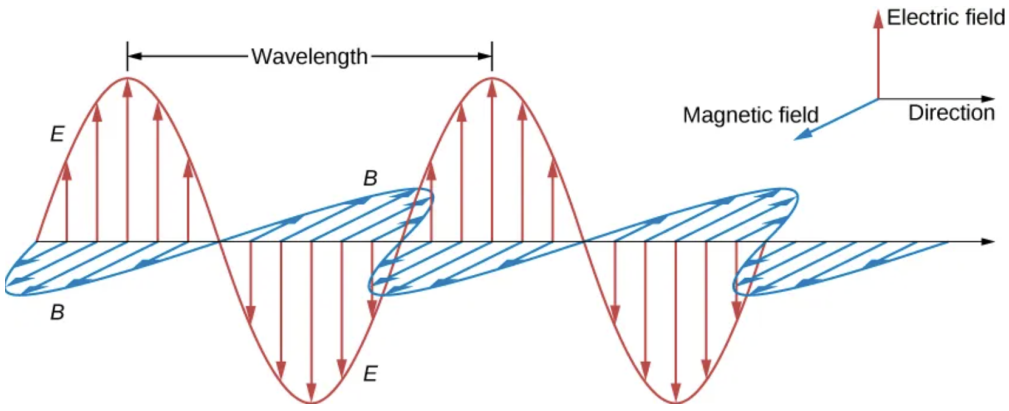

Figure 2.1 – Depiction of the transverse nature of an electromagnetic wave with oscillating magnetic and electric fields [40].

The propagation of harmonic EM plane waves along the z direction can be described for their respective electric and magnetic fields, and are represented by the following complex wave functions [9, 15, 39]:

$$\boldsymbol{E}(z,t) = E_0 e^{i(kz-\omega t)} \tag{2.1.9}$$

$$\boldsymbol{H}(z,t) = H_0 e^{i(kz-\omega t)} \tag{2.1.10}$$

The form of these equations remains the same for propagation through free space and dielectric media that are homogeneous, isotropic and linear, but there are some key differences that will now be discussed. In both cases, E_0 and H_0 are the corresponding field amplitudes, however their ratio with respective to one another changes from free space to dielectric media. They are related by wave impedance $\eta = \sqrt{\mu/\epsilon}$. In free space, the wave impedance is

$$\eta_0 \approx 377\,\Omega. \tag{2.1.11}$$

In a dielectric medium, assuming $\mu_r \approx 1$, this reduces to

$$\eta = \frac{\eta_0}{n}. \tag{2.1.12}$$

As for the remaining variables, t is time, and the wave number is denoted as k, which in free space propagation is given by $k_0 = \frac{\omega}{c}$, where ω represents angular frequency and c is the speed of light in a vacuum. In a dielectric medium, the wave number becomes

$$k = \omega\sqrt{\mu\epsilon} = n\frac{\omega}{c}, \tag{2.1.13}$$

Where n is the refractive index. The phase velocity thus becomes $v = \frac{c}{n}$.

2.2 Diffraction Grating Theory

2.2.1 Light Diffraction in an Ideal Grating

Having established the fundamentals of EM wave propagation, we now consider the phenomenon of light diffraction through a grating. The grating equation for an ideal or classical grating will be derived in its geometric and vector forms to explain the basic mechanism of diffraction. Figure 2.2 below depicts a magnified view of a plane reflection grating which is conceptually analogous to a double-slit configuration. The zoomed-out or macroscopic configuration of this figure would consist of a large number of periodically spaced grooves, but for simplicity only two grooves are shown. Here, we examine the interaction of two equivalent light rays with the grooves, in which the beams strike them at an arbitrary incidence angle θ_i relative to the normal, and diffract at an angle θ_m. The grating spacing or grating period is denoted as a in this figure, however it will be referred to as Λ for the rest of this thesis.

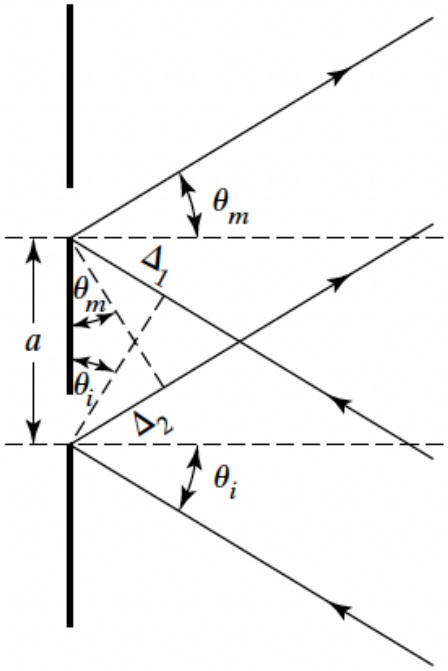

Figure 2.2 – Close-up of a simple reflection grating schematic [38].

The path lengths of the first and second ray in the above figure are denoted Δ_1 and Δ_2, however they will be referred to Δ_i and Δ_m in the following derivations, where i and m denote the respective incident and diffracted rays. The total path difference Δ_T between these equivalent reflected rays from consecutive groove reflections can be mathematically described as follows [38, 41, 42]:

$$\Delta_T = \Delta_i + \Delta_m = \Lambda \sin\theta_i + \Lambda \sin\theta_m \tag{2.2.1}$$

When these beams interfere constructively, $\Delta_T = m\lambda$ which gives us the reflection grating equation that can be written as [5, 9]:

$$\Lambda\left(\sin\theta_i + \sin\theta_m\right) = m\lambda, \quad m = 0, \pm 1, \pm 2, \ldots \tag{2.2.2}$$

Where m represents the diffraction order. The grating equation can also be written in terms of the magnitude of the wave vector $k = \frac{2\pi}{\lambda}$. By dividing both sides of the grating equation by Λ and rearranging so that the equation is in terms of $\sin\theta_m$, we can then multiply both sides by k which results in

$$k\sin\theta_m = k\sin\theta_i \pm \frac{km\lambda}{\Lambda} \tag{2.2.3}$$

We can then substitute $k = \frac{2\pi}{\lambda}$ in the last term of this equation to obtain

$$k\sin\theta_m = k\sin\theta_i \pm \frac{2\pi m}{\Lambda} \tag{2.2.4}$$

And since the magnitude of the grating vector K is represented by $K = \frac{2\pi}{\Lambda}$, the momentum or wave vector form of the grating equation for an ideal diffraction grating can be written as

$$k \sin \theta_m = k \sin \theta_i \pm Km \tag{2.2.5}$$

To aid in visualizing the creation of diffraction orders, Figure 2.3 illustrates this process in reflection and transmission [41].

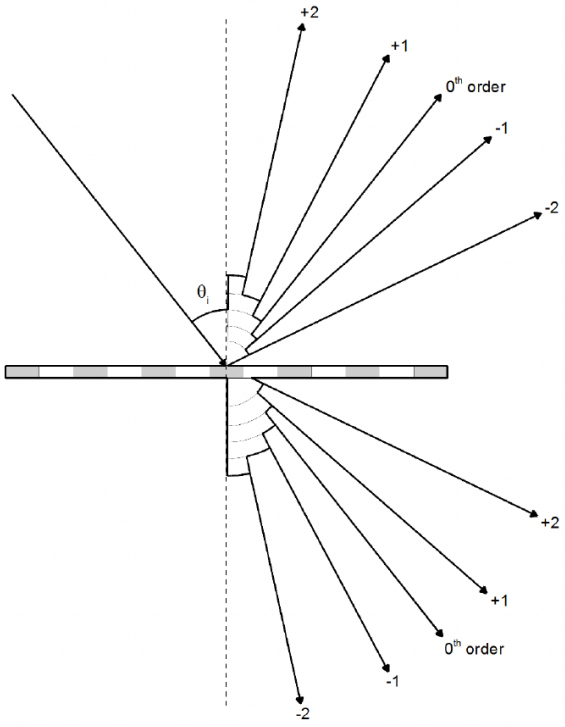

Figure 2.3 – Diffraction orders in reflection and transmission [41].

2.2.2 Light Diffraction in Parallel-Superimposed Gratings

The wave vector form of the diffraction grating equation for a single reflection grating has been presented, and now we can modify this equation to account for parallel-superimposed (PS) gratings. When multiple gratings of varying pitch are inscribed atop one another, the Km term presented in equation 2.2.5 must be modified to account for these variations. Since there is more than one grating in this case, the subscript n is introduced for each variable to represent the number of PS gratings. The term can thus be expressed as

$$K_n m_n = \frac{2\pi m_n}{\Lambda_n}, \quad m_n = \pm 1, \pm 2, \pm 3, \ldots \tag{2.2.6}$$

Where K_n represents the grating vector for a given PS grating, m_n represents its respective diffraction orders, and Λ_n is the corresponding grating pitch for a particular grating inscription in the stack. The term $K_n m_n$ thus represents the discrete momentum transfer provided by the PS grating. In PS gratings such as the stacked MSPGs in this thesis, the total momentum transfer is represented as a summation of the $K_n m_n$ terms. This summation can be written as follows:

$$\sum_{n=1}^{N} K_n m_n = \frac{2\pi m_1}{\Lambda_1} + \frac{2\pi m_2}{\Lambda_2} + \frac{2\pi m_3}{\Lambda_3} + \cdots + \frac{2\pi m_N}{\Lambda_N} \tag{2.2.7}$$

Another important distinction must be made to adjust this equation to the work in this thesis. This equation is general as it accounts for all potential diffraction orders, so we must determine which of these orders are physically allowed and adjust the above equation accordingly. This is accomplished by determining the orders for which a real diffraction angle exists. To do this, we must first go back to the grating equation 2.2.5. At normal incidence, it may be rearranged as follows

$$\sin\theta_m = \frac{m\lambda}{n\Lambda} \tag{2.2.8}$$

Where n represents the index of refraction of the azobenzene thin film and can be approximated as $n \approx 1.57$. A diffracted order will exist only when $|\sin\theta_m| \leq 1$, which implies the condition $|m|\lambda \leq n\Lambda$. In this work, the fabricated MSPG pitches ranged from 376 nm to 548 nm which gives $n\Lambda \approx 590$ nm to 860 nm. Over this band, the first diffraction order ($m = \pm 1$) can satisfy equation 2.2.8 depending on the pitch, whereas the second order ($m = \pm 2$) requires $|2|\lambda \leq n\Lambda$, i.e. $|\lambda| \leq n\Lambda/2 \leq 430$ nm, which does not satisfy the condition. Consequently, within the azobenzene film and for the wavelengths of interest in this thesis, only the zeroth and first diffraction orders are physically allowed ($m = 0, \pm 1$). To account for this first order distinction, equation 2.2.7 can be expressed as

$$\sum_{n=1}^{N} K_1 m_1 = \pm\frac{2\pi}{\Lambda_1} \pm \frac{2\pi}{\Lambda_2} \pm \frac{2\pi}{\Lambda_3} \pm \cdots \tag{2.2.9}$$

Furthermore, all experimental spectroscopic data pertaining to these MSPGs were taken normal to the grating plane (at an incident angle of $\theta_i = 0°$). As such, the wave vector form of the grating equation 2.2.5 for the MSPGs in this work becomes

$$k\sin\theta_m = \pm\frac{2\pi}{\Lambda_1} \pm \frac{2\pi}{\Lambda_2} \pm \frac{2\pi}{\Lambda_3} \pm \cdots \tag{2.2.10}$$

Where Λ_n ranges from $N = 1$ to $N = 10$ in this work. To visualize the PS schematic simply, Figure 2.2.2 depicts an example of light ray propagation in reflection and transmission upon interaction with a bi-grating in terms of grating pitch distribution.

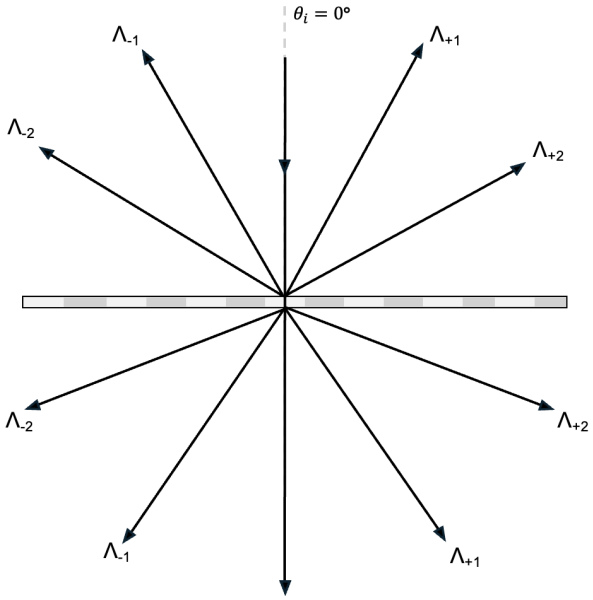

Figure 2.4 – Pitch distribution upon light ray interaction with a bi-grating.

2.2.3 Diffraction Efficiency

An important aspect of diffraction grating theory is diffraction efficiency. Also known as grating efficiency, it can be described as the distribution of light energy of a given wavelength into the various spectral orders [6]. The more distribution of energy into a particular spectral order corresponds to higher efficiency. For the work in this study, it is desirable to obtain as much diffraction efficiency as possible as it enhances coupling, thereby increasing the modulation depth and spectral enhancement. This translates to sharper and deeper reflection peaks in spectroscopic measurements. The efficiency depends on a variety of factors, including the irradiance and polarization of incident light, incident and diffraction angles, refractive index at the grating surface, grating pitch and profile. In this study, efforts were made to increase the diffraction efficiency by optimizing the MSPG fabrication process such that their corresponding reflection spectroscopy peaks were as uniform, deep, and sharp as possible. This was mainly done by varying the grating pitches and inscription times, and further details of these optimization methods will be discussed in the next chapter.

2.3 Waveguide Diffraction Grating Optics

2.3.1 Guided Mode Formation and Coupling

The grating equations presented earlier describe the relationship between incident and diffracted rays, and how various parameters such as incidence angle, diffraction order, and grating pitch affect the angular distribution of light upon grating interaction. However, these equations alone do not describe the mechanism of coupling light into a guided mode. This is necessary to achieve the in-plane momentum condition, which results in the desired spectroscopic grating response at target wavelengths, i.e. reflection peaks. To fully understand the effect of diffraction gratings on EM wave propagation, it is important to discuss phase matching, coupling, and the dispersion relation.

In order for light to be trapped or coupled into a grating, it must satisfy the phase matching condition to be guided into one or more propagation or coupling modes. In a planar (slab) waveguide, guided modes are characterized by the propagation constant β, which may be written as

$$\beta = n_{\text{eff}} k_0 \tag{2.3.1}$$

Where n_{eff} is the effective refractive index of the mode. For guided modes, $n_{\text{eff}} > 1$ which means the value of β is larger than the in-plane momentum available to free space propagation at the same frequency. This inconsistency represents a momentum mismatch which prevents direct coupling of EM waves from free space into guided modes. To correct this mismatch, the grating must increase the momentum of light by providing discrete in-plane momentum increments via the grating vector K_n. This ensures that the propagation constant $\beta > n_c k_0$, where n_c is the refractive index of the cladding (air) and k_o is the wave vector for light traveling in free space. When phase matching occurs, this propagation constant β is equivalent to the in-plane or tangential vector component k_x. Since the work in this thesis was taken at normal incidence and only accounts for the first diffraction order, the wave vector equation 2.2.10 can be made equivalent to β such that

$$\beta = \pm\frac{2\pi}{\Lambda_1} \pm \frac{2\pi}{\Lambda_2} \pm \frac{2\pi}{\Lambda_3} \pm \cdots \tag{2.3.2}$$

Recall that the right side of this equation represents the expansion of the summation of the grating vector term $K_n m_n$. Due to the positive and negative variations, there are two possible solutions of β that only occur when this value matches that of the grating vector term. These solutions can be achieved by changing either the angle of incidence θ_i, the wavelength of incident light λ_0 or the grating pitch Λ. These two solutions dictate whether propagation will occur at discrete intervals, and correspond to forward (positive x direction) or backward (negative x direction) in-plane momentum 'kicks'. These intervals also represent coupling modes that occur at slightly different wavelengths, translating to two separate spectroscopic peaks for a given mode.

2.3.2 Dispersion Curves

To visualize this in-plane addition and subtraction of momentum, a dispersion curve may be used (see Figure 2.5 below). Dispersion is the relationship between energy and momentum, and can be graphically represented in k space by plotting the angular frequency of an EM wave ω as a function of the wave vector component k_x. The uniform and linear light line serves as a reference that represents this dispersion relation in free space, where there is no addition or subtraction of momentum due to a grating. The equation for the light line is

$$\omega = c|k_x| \tag{2.3.3}$$

The forward and backward momentum shifts correspond to grating-assisted coupling modes, and are graphically represented by points of intersection on the dispersion curve. For a typical diffraction grating, there are three intersection points on the dispersion curve which correspond to phase matching or coupling in the backward, normal and forward directions. These intersection points define the experimentally observed resonance wavelengths and thus correspond to distinct spectral features such as reflection peaks. Figure 2.5 (a) illustrates this concept in the positive k_x direction for a sample triple MSPG grating ($N = 3$) at an arbitrary and non-zero angle of incidence θ_i. The dispersion curve for the work in this thesis is even simpler as the incidence angle is zero,

which means only two values of β exist and there is only one point of intersection per grating on the absolute value dispersion curve. Figure 2.5 (b) depicts this effect, specifically highlighting how the light line changes for both cases.

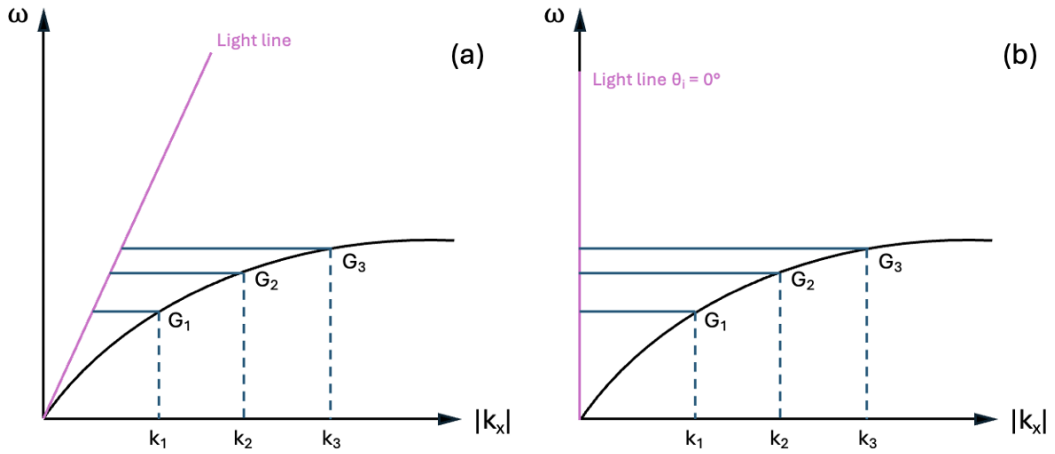

Figure 2.5 – Example of a dispersion curve for a triple MSPG grating ($N = 3$) at an arbitrary, non-zero angle of incidence (a) and at a zero degree incidence angle (b), illustrating the grating-assisted momentum boost that enables coupling at specified target wavelengths.

2.3.3 Retroreflection

Waveguide diffraction gratings such as the MSPGs in this research can be engineered to retroreflect EM waves for the purpose of signature enhancement. Retroreflection occurs when an optical device reflects incident light back to its source, and typical retroreflectors include simple geometric designs such as corner-cubes and spheres. However, grating-based retroreflectors have grown in popularity due to several advantages such as their small size, tunability, and light enhancement capability. Since retroreflection is an application of coupling, grating-based retroreflectors can only couple light into a guided mode when the aforementioned phase-matching condition is met. To ensure the light is decoupled or out-coupled back to its source (such that $\theta_i = \theta_m$), dispersion curves may be used to determine the appropriate grating pitches and backscatter angles.

In recent literature, a gold-coated surface relief bi-grating structure was used to produce both monochromatic and multi-wavelength retroreflection via in- and out-coupling [35]. These bi-gratings were fabricated to retroreflect an arbitrary but specific wavelength of light (785 nm) at various angles, which was a novel achievement. The first grating pitch was designed to in-couple the target wavelength of light in a forward-propagating direction at an arbitrary and pre-determined positive angle θ, identified via a dispersion curve. The second grating pitch was designed to match the SPR phase to out-couple that same wavelength in the reverse direction, such that the magnitude of θ was identical but the sign was negative. Figure 1.4 depicts this monochromatic retroreflection process.

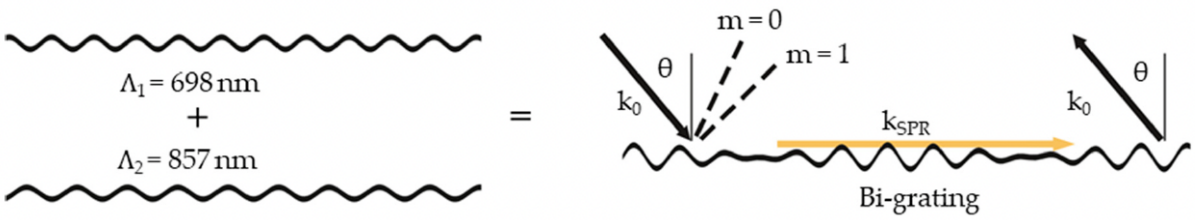

Figure 2.6 – Visualization of the monochromatic retroreflection process for a bi-grating engineered to retroreflect at an arbitrary target wavelength of 785 nm [35].

In comparison, the MSPGs in this work were designed to retroreflect up to ten target wavelengths at normal incidence to achieve broadband and narrowband signature enhancement in the widest possible optical bandwidth. Each grating in-couples and de-couples light at normal incidence ($\theta_i = \theta_m = 0$), such that each 'stacked' grating within an MSPG acts as an independent retroreflector. Normal incidence was selected as it was ideal for establishing a clear proof of concept for MSPG retroreflection. However, spectroscopic measurements could have been taken at alternative angles of incidence to observe additional retroreflections. This represents a promising experimental direction for future work to build upon this research.

2.4 Fourier Analysis

In the previous section, the concept of diffraction efficiency was introduced as a measure of a grating's effectiveness in redistributing optical power. To understand the mechanism governing this process, it is useful to characterize the spatial amplitudes and frequencies of the grating profile given its periodic structure. We can do so by utilizing tools from Fourier optics such as the Fourier transform, and in practice its algorithmic and quicker alternative, the Fast Fourier Transform (FFT).

The Fourier transform can be denoted as $\mathcal{F}\{g\}$, and it decomposes a periodic or harmonic time-based function into a sum of its constituent oscillatory sine and cosine functions, where each component is associated with a specific spatial frequency and amplitude [43]. This is accomplished by taking the integral of a complex function, which is commonly expressed by the equation

$$\mathcal{F}\{g\} = \int_{-\infty}^{\infty}\int_{-\infty}^{\infty} g(x,y)\ \exp[-j2\pi(f_x x + f_y y)]\ dx\,dy \tag{2.4.1}$$

Where $g(x,y)$ is a general, complex-valued and 2D function of the independent variables x and y, and f_x and f_y generally represent the frequencies.

However, in the case of this MSPG research, only a one dimensional (1D) analysis is required to extract each grating's amplitude and spatial frequencies. A 1D FFT of the multi-superimposed surface grating profiles was thus performed, and the previous equation changed to

$$\mathcal{F}\{g\}(f_x) = \int_{-\infty}^{\infty} g(x)\ \exp(-j2\pi f_x x)\ dx \tag{2.4.2}$$

From this information, the modulation depth of the spectroscopic reflection peaks can be identified. In doing so, insight into its diffraction efficiency is gained as deeper gratings are correlated to better coupling, and thus higher efficiency. The FFT is thus an efficient and reliable method of determining the periodicity and depth of a grating as a means of optimizing its performance; that

is, ensuring the constituent signals of each parallel-superimposed grating are as uniform or equal as possible.

Chapter 3

Experimental Methods

This chapter details the experimental methods that were used to carry out the goal of this work as described in the thesis statement. These methods were employed to obtain the desired results presented in the next chapter, as well as to validate the aforementioned theory. This section presents a comprehensive overview of the multi-superimposed parallel grating (MSPG) fabrication process, including the means by which they were manufactured to achieve discrete and continuous spectral enhancement in the optical regime. Finally, this chapter describes the post-fabrication analysis which is the basis of the results, including spectroscopic data collection and grating surface characterization.

3.1 Thin Film Sample Preparation

A Disperse Red 1 (gDR-1) azobenzene and mexylaminotriazine compound was synthesized according to literature [44]. This synthesis results in a fine powder that can then be dissolved in a liquid dichloromethane (CH_2Cl_2) solution with a 3 wt% mix ratio. The solution was mixed via shaking for approximately one hour before being filtered through a 50 μm syringe to remove any larger particulates. Corning brand soda lime glass slides were then cut into squares of 3×3 cm, cleaned with dish soap and lukewarm water, and dried using Kim wipes to minimize the presence of surface particles such as dust. The slides were then placed in an oven set to 85°C for a minimum of five minutes to ensure that any remaining water was evaporated from the surface. The prepped slides would then be blown with compressed air before being placed in the humidity-controlled spin-coating chamber. A pipette is used to deposit 3 mL of the azobenzene-containing solution on each slide, which is then spun at 1200 revolutions per minute (RPM) for 35 seconds to evenly coat the glass substrate. This aforementioned process produces a thin film thickness of approximately 300 to 400 nm that is ideal for grating inscription.

3.2 Multi-Superimposed Parallel Grating Fabrication

3.2.1 Lloyd Mirror Interferometer Setup

As discussed in Chapter 1, the diffraction gratings required for this thesis are holographic surface relief gratings (SRGs), which can be created using a process known as laser interference lithography (LIL). This technique can utilize the photoisomerization property of azobenzene to alter its molecular structure in the presence of light, thereby producing a sinusoidal grating profile

which is ideal for efficient first order coupling and diffraction. To create this interference periodic fringe pattern, a Lloyd mirror interferometer configuration was used.

As shown in Figure 3.1 below, this setup consists of a coherent Verdi 2025 diode-pumped 532 nm wavelength laser which is passed through a spatial filter and collimated with a convex lens in order to parallelize and narrow the beam. A quarter-wave plate is placed in front of the collimating lens to generate circularly polarized light. This wavelength and polarization combination has been experimentally proven as being the most efficient for writing gratings in azobenzene-coated thin films, as it ensures the azobenzene molecules can absorb this wavelength of light and undergo the necessary cis-trans isomerization to create SRGs, regardless of their orientation [41, 42]. An adjustable iris was placed in front of the quarter-wave plate to control the diameter of the incident light beam on the substrate. The laser light, with an average irradiance of $300\,\mathrm{mW/cm^2}$ as measured using a Coherent Power-Max sensor, then reaches the azobenzene sample which is placed orthogonally to a mirror and mounted on a rotating stage to that facilitates manual pitch control. The 90° geometry between the sample and mirror ensures that half of the incident light directly reaches the sample while the other half reflects off the mirror before reaching the same portion of the sample, thus creating a spatially periodic intensity distribution [9].

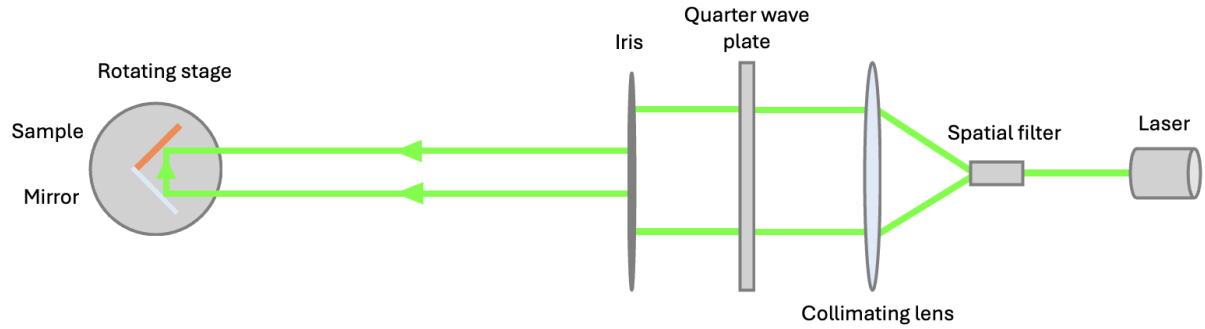

Figure 3.1 – Lloyd mirror interferometer setup.

As the angle of the stage changes, so does the resulting grating pitch. This is shown by Equation 3.2.1 below, which can be derived from two-beam interference and irradiance theory [38, 45].

$$\Lambda = \frac{\lambda}{2\sin\theta} \tag{3.2.1}$$

The pitch Λ is directly dependent on the wavelength of the laser λ, and the angle θ between the direct and reflected beams and the sample surface normal. The resulting light and dark fringe pattern can thus have a smaller or larger spacing depending on the angle. Regardless of this angle, in this particular Lloyd setup the pitch is spatially uniform, meaning a constant pitch is maintained throughout the grating.

3.2.2 Grating Inscription

Recall from Chapter 1 that the goal of this research is to achieve signature enhancement in the optical regime by widening the bandwidth of wavelength-selective reflection modes. To accomplish this, two strategies were employed. The first strategy was hypothesized and experimentally demonstrated to generate as many discrete spectral responses as possible in the visible range by 'stacking' or parallel-superimposing multiple gratings until the maximum number of reflection peaks

is achieved, hence the term MSPG. The second strategy involved converging these discrete peaks into a singular, continuous peak by systematically reducing the spacing between adjacent target reflection wavelengths. Although a broadband result was anticipated, the converged modes actually produced narrowed composite peaks, which is still a useful result and will be further discussed in the next chapter. To fabricate both types of MSPGs, the stage in the Lloyd's mirror setup would be electronically rotated to a particular angle based on the desired grating pitch Λ. This was determined by the following derivation. From Equation 2.3.1 we know that

$$n_{\text{eff}} k_0 = \frac{2\pi}{\Lambda} \tag{3.2.2}$$

Given that the wave vector $k_0 = \frac{2\pi}{\lambda}$, we can substitute k_0 into Equation 3.2.2, and through the cancellation and rearranging of terms obtain

$$\Lambda = \frac{\lambda}{n_{\text{eff}}} \tag{3.2.3}$$

Which is the equation used throughout the research to determine the desired experimental pitch values. In this equation, $\lambda = \lambda_{\text{t}}$ where λ_{t} represents the target reflection wavelengths. The value n_{eff} is the effective index of refraction experienced by light propagating through the waveguide. Using the basic condition for a slab waveguide $n_{\text{core}} > n_{\text{eff}} > n_{\text{cladding}}$, this can be adapted for the work in this research and rewritten as

$$n_{\text{azo}} > n_{\text{eff}} > n_{\text{substrate}} > n_{\text{air}} \tag{3.2.4}$$

Where the approximation $n_{\text{azo}} \approx n_{\text{eff}}$ can be made, since the first diffraction order ($m = \pm 1$) is the only order that can satisfy Equation 2.2.8 as derived in Chapter 2.2.2. The estimated refractive index for azobenzene was $n_{\text{azo}} = 1.57$, and given the above approximation, the effective refractive index used in Equation 3.2.3 was $n_{\text{eff}} = 1.57$. Given this value, and the target reflection wavelengths λ_{t} which ranged from 590 nm to 860 nm, the experimental grating pitches Λ thus varied between 376 nm and 548 nm. Values beyond these lower and upper boundaries were experimentally determined to produce a level of spectrometric signal noise that was difficult to distinguish from real reflection peak data.

The discrete MSPG inscription method can be described by examining their fabrication parameters. As an example, Table 3.1 below contains the experimental data required to produce single, bi, triple, quadruple, and quintuple MSPGs ($N = 1, 2, 3, 4, 5$). A complete list of parameters for the remaining $N = 6$ to $N = 10$ MSPGs is provided in Appendix A.1. Note that the single grating was made as a reference to provide continuity, and as such is not considered an MSPG.

Table 3.1 – Target fabrication parameters for the primary or 'discrete' method for single to quintuple MSPGs. All gratings were inscribed at a constant irradiance of $I = 300\,\mathrm{mW/cm^2}$.

N	Grating	λ_t (nm)	$\Delta\lambda_t$ (nm)	Λ_t (nm)	T (s)
1	G1	650	30	414	200
2	G1	650	30	414	200
	G2	680		433	90
3	G1	650	30	414	200
	G2	680		433	90
	G3	710		452	60
4	G1	650	30	414	200
	G2	680		433	90
	G3	710		452	60
	G4	740		471	45
5	G1	650	40	414	200
	G2	690		440	60
	G3	730		465	60
	G4	770		490	60
	G5	810		516	60
		⋮			
Parameters for $N = 6$ to $N = 10$ are shown in Appendix A.1.					

In each of these MSPGs, the individual grating layers were inscribed to achieve a specific target wavelength by manually controlling the corresponding grating pitch. For example, G1 was often fabricated to achieve $\lambda_t = 650$ nm by using $\Lambda = 414$ nm. Once the sample was mounted on the stage in accordance with the previously described Lloyd's mirror setup, this pitch value would be manually entered in the LabView software and the stage would then electronically rotate to the corresponding angle. All gratings were inscribed with a laser power (P) of 2 W and irradiance (I) of 300 $\mathrm{mW/cm^2}$, with sequentially decreasing inscription times. Two sets of inscription times were developed, the first denoted as Version 1 (V1) and characterized by the exposure times G1= 200s, G2= 60s, ..., GN= 60s (for $N = 5$ to $N = 10$). The second is known as V2 and was utilized for $N = 1$ to $N = 4$ as it produced more uniform reflection peaks compared to the V1 method. The V2 times were G1= 200s, G2= 90s, G3= 60s, G4= 45s. These power and time combinations were determined during the optimization process and will be further described in the results section. For the second grating G2, the stage would be rotated to a different angle that aligned with the next pitch (e.g. $\Lambda = 433$ nm) which was determined from the preselected target wavelength (e.g. $\lambda_t = 680$ nm). The ideal difference between target wavelengths ($\Delta\lambda_t$) for G1, G2, G3, ..., G10 was experimentally determined to be either 30 nm or 40 nm. This separation distance ensured that no overlap occurred between reflection peaks while allowing for the maximum number of discrete peaks across the detectable reflection bandwidth ($\lambda_t \approx$ 590-860 nm).

The secondary 'continuous' MSPG inscription strategy was tested by reducing the spacing between adjacent target reflection wavelengths until the peaks converged. The aforementioned MSPG fabrication method was also employed for this peak convergence strategy, however $\Delta\lambda_t$ did not range from 30-40 nm as it did in the first method. Instead, this separation distance was incrementally reduced by various distances to observe how close the peaks could be brought together before they fully merge. This started at 15 nm, then 10 nm, and finally 5 nm which was found to be the minimum separation distance that did not exceed the resolution threshold of

the OceanView spectrometer, and produced the most precise merging. Figure 3.2 below visually depicts this process for a bi MSPG ($N = 2$), and it is clear that the minimum separation distance corresponds to the closest possible merging of adjacent resonances. Note that this process was repeated for the remaining MSPGs ($N = 3$ to $N = 10$), and that the results presented in Chapter 4 only include MSPGs fabricated with the minimum separation distance of $\Delta\lambda_t = 5$ nm.

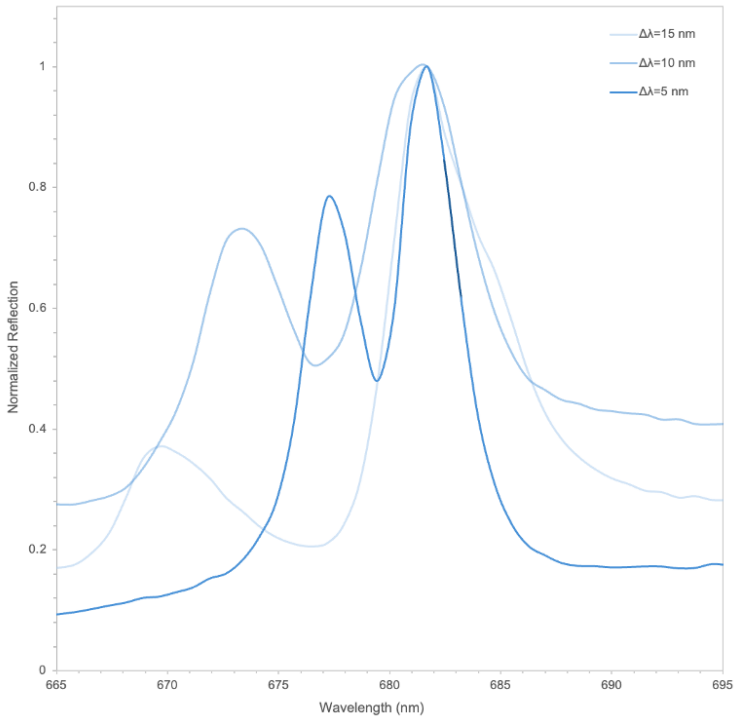

Figure 3.2 – Magnified overlay of incrementally decreasing wavelength separation distances ($\Delta\lambda = 15, 10, 5$ nm) for a bi MSPG ($N = 2$) using the continuous fabrication method.

A list of full fabrication parameters for this method is shown in Table 3.2 below for $N = 2$ to $N = 5$ as an example. The parameters for the remaining $N = 6$ to $N = 10$ MSPGs are located in Appendix B.1.

Table 3.2 – Target fabrication parameters for the secondary or 'continuous' method for bi to quintuple MSPGs. All gratings were inscribed at a constant irradiance of $I = 300\,\mathrm{mW/cm^2}$.

N	Grating	λ_t (nm)	$\Delta\lambda_t$ (nm)	Λ_t (nm)	T (s)
2	G1	650	5	414	200
	G2	655		417	90
3	G1	650	5	414	200
	G2	655		417	90
	G3	660		420	60
4	G1	650	5	414	200
	G2	655		417	90
	G3	660		420	60
	G4	665		424	45
5	G1	650	5	414	200
	G2	655		417	60
	G3	660		420	60
	G4	665		424	60
	G5	670		427	60
			⋮		
Parameters for $N = 6$ to $N = 10$ are shown in Appendix B.1.					

3.3 Spectral Analysis

Once the MSPGs are fabricated, their spectral responses can be characterized by reflection spectroscopy. These responses manifest as distinct peaks in the measured reflection spectra and can be interpreted as a unique identifier or spectral 'fingerprint' for each fabricated structure. The MSPG samples are illuminated with broadband (white) light, thus enabling the occurrence of wavelength-selective diffraction and coupling effects. The reflected signal is then collected and measured with a spectrometer, and displayed on its corresponding software as a function of intensity versus wavelength. In this graphical representation, peaks in the reflection spectrum correspond to wavelengths that satisfy the phase-matching condition for grating-assisted coupling into and out of guided modes supported by the MSPGs via the azobenzene thin film. The measured peak positions can then be compared to the designed target wavelengths to determine whether the MSPGs successfully achieved the intended wavelength-selective coupling behavior.

The spectrometer setup shown in Figure 3.3 below was used for all data collection in this study and can be described as follows. First, light from a halogen lamp is illuminated through a variable square aperture. A neutral density filter (NDF) is placed in front of the aperture to adjust the intensity or brightness of the light, which is necessary to prevent oversaturation of the signal in the spectrometer. The light then passes through a convex lens which focuses it through the remainder of the optical rail. The light enters a 180° vertically aligned linear polarizer, then passes through another iris with a small diameter of ∼5 mm before reaching a semi-transparent lens. This lens is tilted at an angle such that it transmits the incident light to the sample on the stage, and reflects the light returned from the sample to the final focusing lens. This narrows the beam even more to ∼1 mm such that it fits the aperture dimensions of the OceanView spectrometer. In every data collection conducted for this study, the sample was oriented normal to the incident light such that the grating lines were parallel to the polarization of the incoming light beam. The collected

reflection spectra could then be observed via OceanView software on a reflectance (%R) versus wavelength graph, where each target reflection wavelength or combination thereof would appear as one or more distinct peaks. This graphical data constitutes the core analysis of the results section.

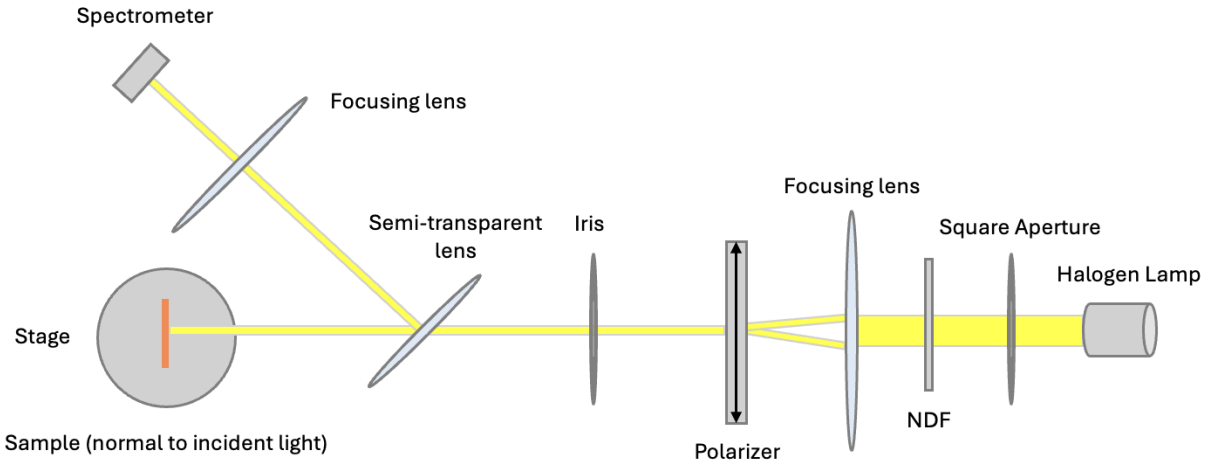

Figure 3.3 – Spectrometer setup for reflection spectra measurement.

3.4 Surface Characterization

3.4.1 Atomic Force Microscope Imaging

The surface of every MSPG was scanned with an atomic force microscope (AFM) to observe and analyze a variety of factors, including but not limited to: the uniformity of reflection peaks, grating modulation depth, surface profile, and spectral periodicity or pitch. The AFM used in this research is from Bruker (Massachusetts, USA), and its trademark PeakForce Tapping feature enables the aforementioned sample analysis. This mode involves the periodic modulation of a tiny metal needle tip called a probe, which taps the sample with a piconewton (pN) force [46]. This ultra-low interaction force and modulation frequency is measured by the probe's deflection off the surface, which allows for extremely high precision imaging down to the nanometer level while maintaining the structural integrity of the sample. The probe scans along the sample in accordance with preselected parameters such as resolution, scan range, and scan rate. The Bruker AFM software then uses this data to construct multi-dimensional maps or images of the grating surface, such as the example in Figure 1.4 below. From these images, the aforementioned surface characteristics can be extracted and further analyzed in the software directly, or externally with the NanoScope Analysis software [42, 47].

In this work, each MSPG sample was analyzed in a similar way. To ensure the gratings were inscribed well and that their fringe patterns were constant-pitched or uniform throughout the grating surface, three different scans were taken at multiple reference points on each sample, starting at the left edge of the grating and approximately in the middle. The second scan would be taken 500 μm to the right of the first scan, and the third would be taken 500 μm to the right of the second scan. The resolution would be set to 256 samples per scanning line, with a scan rate of 0.5 Hz to 1 Hz and a respective scan range of 10 μm to 25 μm. These two scan range and rate combinations were tested in each sample to determine their effectiveness. The combination that yielded superior

results for a particular sample would be selected for further analysis and is subsequently presented in the results section. Figure 3.4 shows an example of an AFM image for a quintuple MSPG ($N = 5$) with a scan rate of 1 Hz and a 10 μm scan range. These 2D and 3D cross-section scans are unique to each MSPG, as they represent the resultant profile created from the superposition of each PS grating's individual sinusoidal profile [35].

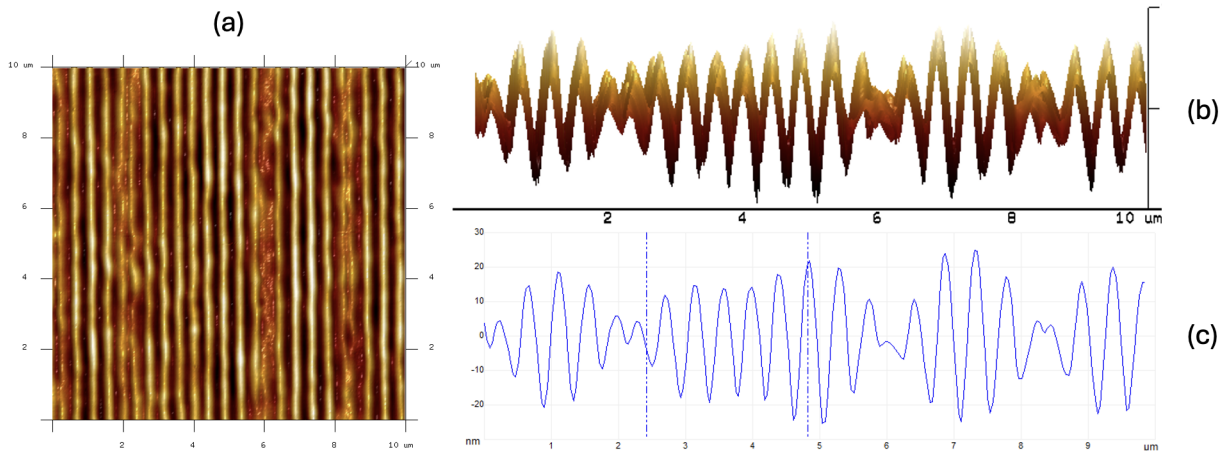

Figure 3.4 – Example of multi-dimensional AFM imaging showing the surface profile and analysis of a quintuple ($N = 5$) MSPG from the overhead point of view (a), and side-on cross-sections in 3D (b) and 2D (c).

Chapter 4

Results and Discussion

As previously stated, the main goal of this research was to achieve broadband signature enhancement in the optical regime. This was accomplished by developing and testing parallel-superimposed (PS) grating inscription strategies, which ultimately led to the creation of the novel multi-superimposed parallel grating (MSPG) method. This method achieved the desired results by enabling two distinct spectral filtering effects, resulting in both discrete (broadband) and continuous (narrowband) reflection modes across the detectable optical range. The supporting theory and experimental methods for these MSPGs were previously described in Chapters 2 and 3. This chapter expands upon these concepts by presenting the optimization process, results, and subsequent analysis of these discrete and continuous MSPGs, including limitations and potential improvements. It also considers the broader impact of this research to photonics applications and the field of optics at large, including remote sensing and defence technology.

4.1 Grating Optimization

The goal of grating optimization is to enhance the spectral response of the MSPGs. In this context, spectral enhancement can be defined in several ways, for instance by increasing the resolution, sharpness, and depth of the spectroscopic reflection peaks, and producing discrete reflection peaks that are as uniform in shape and size as possible. Achieving uniformity can equalize the modulation depths, thus resulting in similar diffraction efficiencies for each reflection peak or resonance and enhancing the quality of the spectroscopic data. To optimize MSPGs in these ways, the laser irradiance or grating exposure times could be modified during the inscription process.

The laser power was chosen to remain constant for all MSPG inscriptions at a value of 2 W, with a corresponding irradiance of 300 mW/cm^2. These values were determined to be optimal for fabricating these MSPGs, as lower values would not create large enough modulation depths to enable wavelength-selective coupling, which is necessary for observing the corresponding individual reflection modes. Conversely, if the power or irradiance were too high then it would risk bleaching the azobenzene, thus preventing the critical photoisomerization and laser interference lithography (LIL) processes from occurring. Additionally, it could cause sequential gratings to overwrite or erase the initial gratings in the MSPG stack.

As such, two different exposure time optimization techniques were employed during the grating inscription process. These were determined through a combination of trial and error and understanding previous literature pertaining to the impact of exposure times on PS gratings. The first method, also referred to as the V1 technique as described in Chapter 3, was initially developed for individual gratings within all MSPGs ($N = 1$ to $N = 10$). The grating inscription or exposure

times were as follows: G1= 200s, G2= 60s, G3= 60s, G4= 60s, . . . , G10= 60s. This method worked universally among both discrete and continuous fabrication methods, and produced relatively uniform reflection peaks and ensured that all gratings remained intact i.e. there was no erasing or overwriting of initial gratings. An alternate or V2 time exposure method was found to further enhance the spectral response for $N = 2$ to $N = 4$ MSPGs specifically. These gratings were inscribed using the following decreasing exposure times: G1= 200s, G2= 90s, G3= 60s, and G4= 45s. This approach further increased the discrete reflection peak uniformity and depth as shown in Figure 4.1 below. Variations of the V2 method were attempted for gratings $N = 5$ and beyond but it did not prove as effective as the V1 method, so V1 was employed for $N = 5$ to $N = 10$ MSPGs.

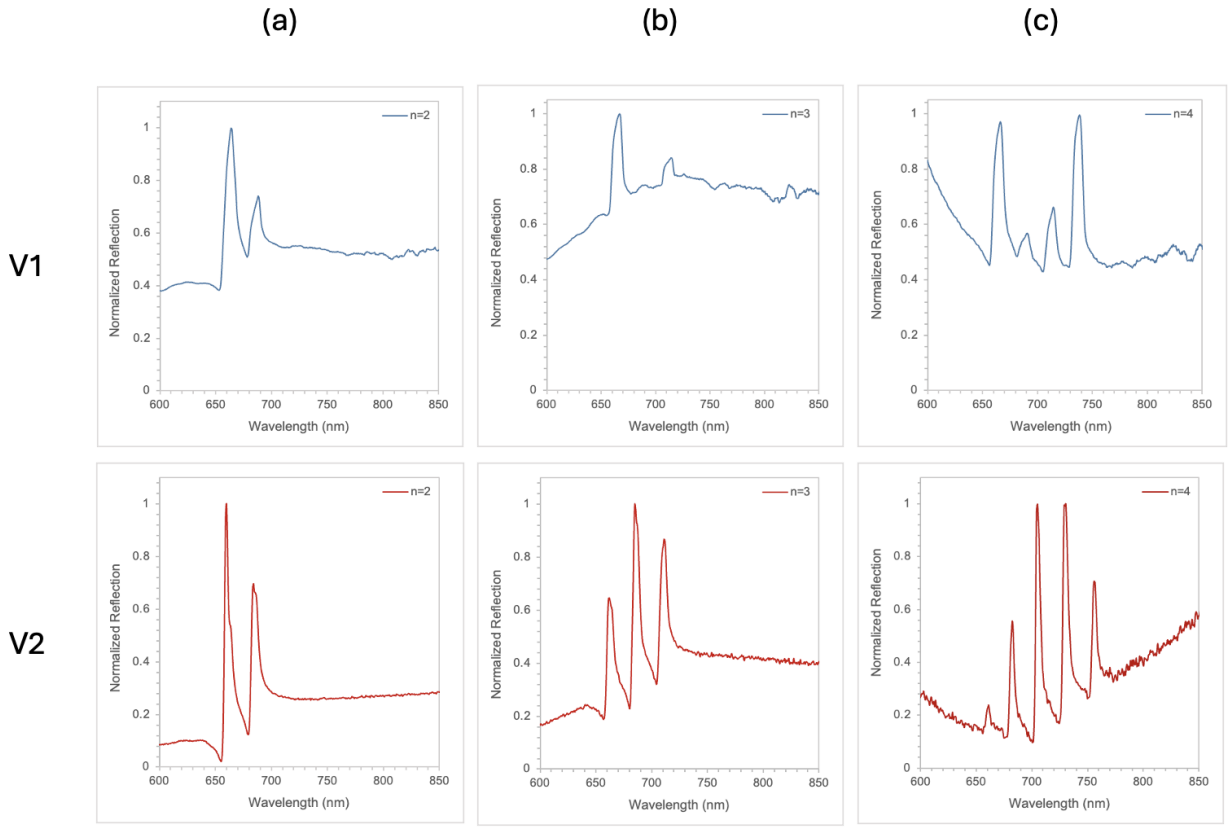

Figure 4.1 – Comparison of V1 (top row) versus V2 (bottom row) time optimization methods for $N = 2, 3, 4$ MSPGs to demonstrate spectral enhancement.

There are a multitude of factors working against these optimization efforts due to the human involvement required during MSPG fabrication, particularly during the spin coating process. The mechanism of spin coating the glass substrates cannot guarantee perfectly uniform azobenzene distribution among the experimental sample set. This can result in uneven azobenzene distribution across the glass substrate, leading to variation in thin film thickness throughout the sample. The spinning process also causes azobenzene to accumulate more towards the edges of the sample rather than in the centre.

4.2 Spectroscopic Data Processing

Before the experimental results are presented, the spectroscopic data processing procedure is first described to explain how the raw reflectance spectra were normalized, baseline-corrected, and prepared for analysis. To ensure that spectroscopic results were analyzed in an accurate and consistent way, raw reflectance data ($\%R$) for both discrete and continuous MSPG methods were processed in Excel using the following workflow. First, the y-axis reflectance data for all MSPGs was normalized from 0 to 1 to standardize the range of values, thus equalizing the scale of intensity across each dataset while preserving relative peak amplitudes. Next, a baseline correction was applied to spectra that exhibited significant sloping. This step served to even out the baseline of the affected datasets, thus facilitating the identification and comparison of reflection peaks within and among MSPG orders. As an example, Figure 4.2 below shows the spectroscopic data before and after the normalization and baseline correction of a quintuple MSPG.

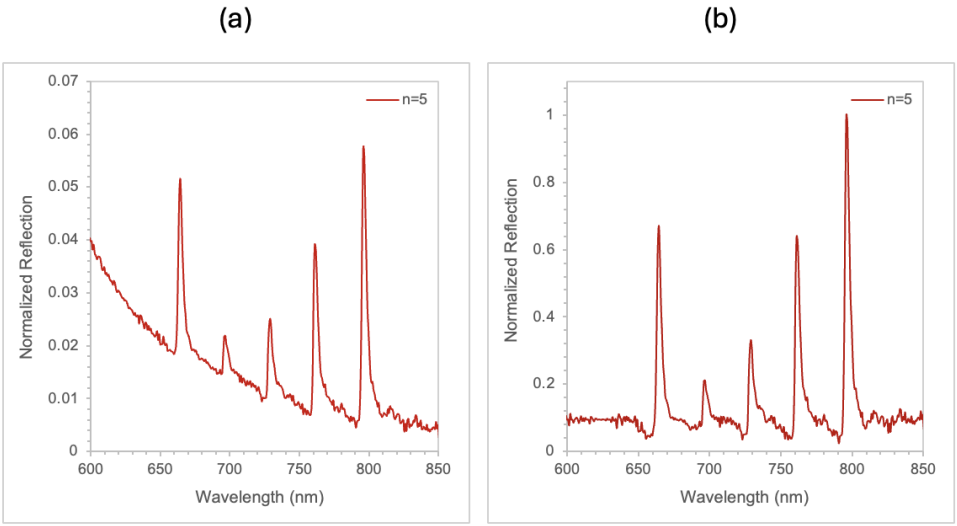

Figure 4.2 – Comparison of spectroscopic reflectance data for a discrete quintuple ($n = 5$) MSPG before normalization and baseline correction (a) and after (b).

For the $N = 1$ to $N = 4$ discrete MSPGs, the normalized spectra exhibited a slight upward slope in the baseline following the primary reflection peaks. This behavior is consistent with azobenzene-enabled coupling effects in which the presence of broadband light on a PS diffraction grating increases the intensity of reflected light, thus producing a gradual rise in the spectroscopic baseline after successive gratings as seen in Figure 4.1. A baseline correction was not performed on these spectra as the post-normalization results were satisfactory. For higher-order discrete MSPG spectra ($N = 5$ to $N = 10$), the normalized reflectance curves exhibited a more significant downward slope that obscured resonance features as N increased. In these cases, the data was normalized twice, once before applying a baseline correction and once after, to systematically remove unwanted background signals while preserving the narrow spectral peaks associated with the MSPG resonances.

As for continuous MSPG spectra ($N = 2$ to $N = 10$), the aforementioned process was also conducted. This consisted of an initial normalization, followed by a baseline correction and final normalization. This process rectified the slight upward sloping and is shown below in Figure 4.3 for a sextuple ($N = 6$) MSPG.

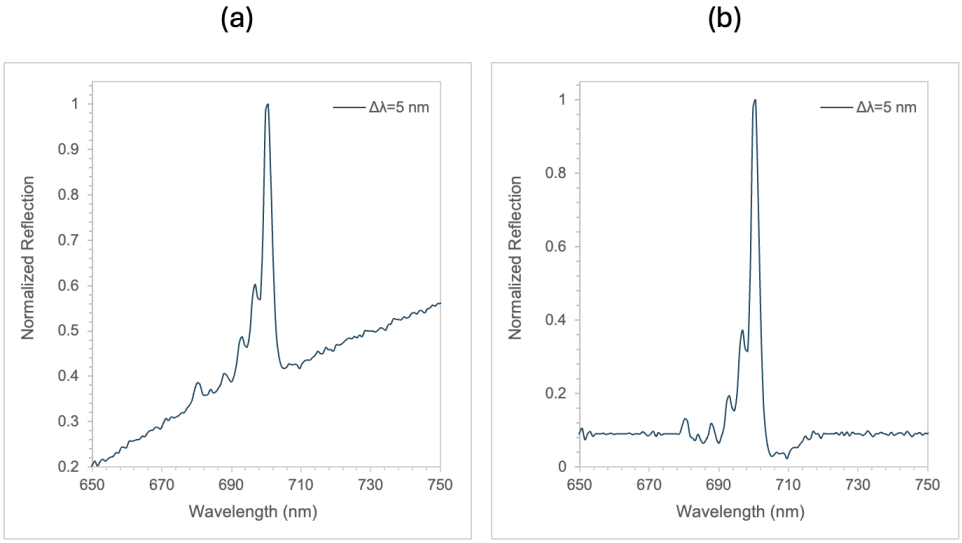

Figure 4.3 – Comparison of spectroscopic reflectance data for a continuous sextuple ($N = 6$) MSPG before normalization and baseline correction (a) and after (b).

Additional detail into the normalization and baseline processing of reflectance spectra will now be provided. First, the recorded raw reflectance signal associated with each wavelength $\%R(\lambda)$ was normalized between the values of 0 and 1 using a min-max equation to place each spectrum on a common relative intensity scale:

$$R_{\text{norm}}(\lambda) = \frac{R(\lambda) - \min(R(\lambda))}{\max(R(\lambda)) - \min(R(\lambda))} \tag{4.2.1}$$

Where R_{norm} denotes the normalized reflectance. The baseline of the normalized reflectance spectrum was then estimated using a rolling median filter, which removed the sloped background signal while preserving the narrow resonance features. For each wavelength point at the ith data point λ_i, the local baseline was calculated as the median reflectance within a symmetric sliding window of 20 data points centered on each wavelength value:

$$B_{norm}(\lambda_i) = \text{median}\left(R_{\text{norm}}(\lambda_{i-20}), \ldots, R_{\text{norm}}(\lambda_{i+20})\right) \tag{4.2.2}$$

Where B_{norm} denotes the baseline correction and i represents the index of the wavelength sample in the discrete reflectance spectrum. This methodology corresponds to a 41-point moving median filter or window applied to the normalized reflectance spectrum. The baseline was then subtracted from the normalized signal to isolate the resonance features as follows:

$$R_{\text{corr}}(\lambda) = R_{\text{norm}}(\lambda) - B(\lambda) \tag{4.2.3}$$

Where R_{corr} denotes the corrected reflectance values post-baseline correction. The use of a median filter followed by this subtraction effectively ignores the narrow resonance peaks thus keeping them intact, which assists in suppressing the sloped background component of the signal to a relatively flat baseline. Finally, the spectrum was renormalized to ensure that all spectra lie within the range

$$0 \leq R_{\text{final}}(\lambda) \leq 1 \tag{4.2.4}$$

The equation to determine the final normalization is as follows:

$$R_{\text{final}}(\lambda) = \frac{R_{\text{corr}}(\lambda)}{\max\left(R_{\text{corr}}(\lambda)\right)} \tag{4.2.5}$$

These steps ensure that all spectra lie within the specified range and that the maximum peak intensity does not exceed unity (1), thus allowing direct visual comparison between different MSPG orders. To further facilitate visual inspection and comparison of the resonance peaks, a final adjustment was applied to most spectra. Since the baseline subtraction can produce negative values for peaks lying directly on the baseline, a small positive offset δ was added to shift up the baseline to maintain positive values:

$$R_{\text{shift}}(\lambda) = \frac{R_{\text{final}}(\lambda) + \delta}{1 + \delta} \tag{4.2.6}$$

The values for δ varied between approximately 0.01 and 0.35 depending on the spectrum, and were chosen such that the baseline remained slightly above zero for visualization purposes. The sequential completion of the aforementioned data processing steps resulted in the final graphs, which are presented in the following section.

4.3 MSPG Spectroscopy Data (Discrete Method)

The results of the first MSPG fabrication method will now be presented, which consists of single to decuple ($N = 1$ to $N = 10$) discrete MSPGs. Recall that the goal of this method was to broaden the reflection bandwidth across the optical regime by creating as many discrete resonances as possible without overlap. Through experimentation, the maximum number of gratings that could be parallel-superimposed without emission peaks overlapping was determined to be ten.

The presentation of the upcoming results are described as follows. For each MSPG, a graph of normalized reflectance ($\%R$) versus wavelength (λ) in nm is presented to demonstrate the recorded spectral response. Each graph has a faint vertical line inserted at the theoretical reflection wavelengths for ease of visual comparison between the theoretical and actual emission peaks.

Additionally, each graph has a corresponding table below it with eight parameters. The first column is N, representing the number of stacked gratings within an MSPG. Next is the grating number (G1, G2, G3, etc.), which represents the order of gratings in the PS 'stack'. Then there is the target wavelength λ_t and separation distance between adjacent target wavelengths $\Delta\lambda_t$. This is defined as

$$\Delta\lambda_t = \lambda_{t,i} - \lambda_{t,i-1} \tag{4.3.1}$$

Where $\lambda_{t,i}$ corresponds to the sequential grating number or order as described above. Next, the measured wavelength λ_m and separation distance between measured adjacent wavelengths $\Delta\lambda_m$ are presented. Similar to above, this is calculated as

$$\Delta\lambda_m = \lambda_{m,i} - \lambda_{m,i-1} \tag{4.3.2}$$

The next parameter is Err_{abs}, which represents the absolute error quantifying the deviation between the wavelengths of the target and measured reflection peaks, and is calculated as

$$\text{Err}_{\text{abs}} = \frac{|\lambda_m - \lambda_t|}{\lambda_t} \times 100\% \tag{4.3.3}$$

The final parameter is $\text{Err}_{\text{spacing}}$, and it quantifies the error of the relative separation distance or spacing between target and measured reflection peaks. This aids in evaluating the fabrication accuracy of the discrete MSPGs and is defined as

$$\text{Err}_{\text{spacing}} = |\Delta\lambda_m - \Delta\lambda_t| \tag{4.3.4}$$

4.3.1 Single Grating ($N = 1$)

The normalized reflectance spectra as a function of wavelength for a single grating ($N = 1$) are presented in Figure 4.4, while the corresponding target and measured resonance wavelengths and associated errors are summarized in Table 4.1.

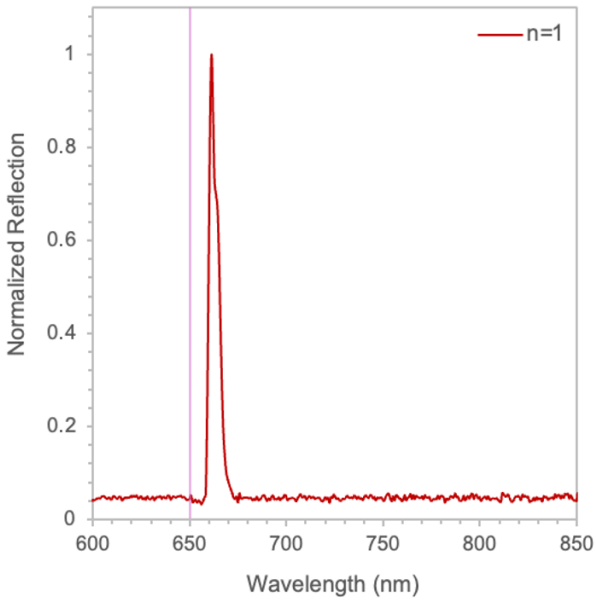

Figure 4.4 – Normalized reflectance spectra versus wavelength for a single grating ($N = 1$) fabricated using the discrete method. The measured resonance wavelength corresponds to that reported in Table 4.1.

Table 4.1 – Target and measured resonance wavelengths for a single MSPG fabricated using the discrete method ($N = 1$).

N	Grating	λ_t (nm)	$\Delta\lambda_t$ (nm)	λ_m (nm)	$\Delta\lambda_m$ (nm)	Err_{abs} (%)	$\text{Err}_{\text{spacing}}$ (nm)
1	G1	650	-	661	-	1.69	-

Note that as a single grating, there is no parallel-superimposition occurring therefore this is not considered an MSPG. This was included in the results for continuity as it serves as a reference grating for the subsequent MSPGs.

4.3.2 Bi MSPG ($N = 2$)

The normalized reflectance spectra as a function of wavelength for a bi MSPG ($N = 2$) are presented in Figure 4.5, while the corresponding target and measured resonance wavelengths and associated errors are summarized in Table 4.2.

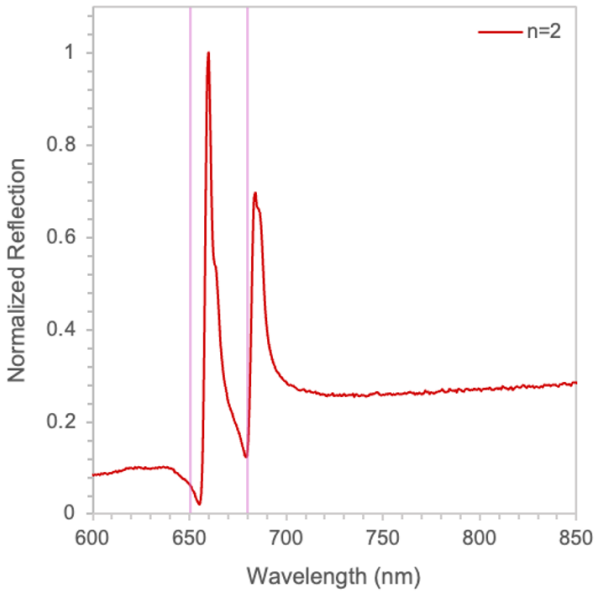

Figure 4.5 – Normalized reflectance spectra versus wavelength for a bi MSPG ($N = 2$) fabricated using the discrete method. The measured resonance wavelengths correspond to those reported in Table 4.2.

Table 4.2 – Target and measured resonance wavelengths for a bi MSPG fabricated using the discrete method ($N = 2$).

N	Grating	λ_t (nm)	$\Delta\lambda_t$ (nm)	λ_m (nm)	$\Delta\lambda_m$ (nm)	$\mathrm{Err}_{\mathrm{abs}}$ (%)	$\mathrm{Err}_{\mathrm{spacing}}$ (nm)
2	G1	650	-	660	-	1.54	-
	G2	680	30	684	24	0.59	6

4.3.3 Triple MSPG ($N = 3$)

The normalized reflectance spectra as a function of wavelength for a triple MSPG ($N = 3$) are presented in Figure 4.6, while the corresponding target and measured resonance wavelengths and associated errors are summarized in Table 4.3.

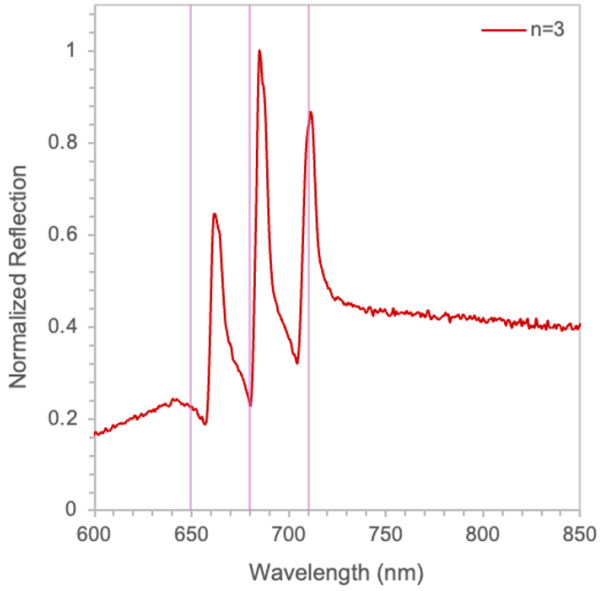

Figure 4.6 – Normalized reflectance spectra versus wavelength for a triple MSPG ($N = 3$) fabricated using the discrete method. The measured resonance wavelengths correspond to those reported in Table 4.3.

Table 4.3 – Target and measured resonance wavelengths for a triple MSPG fabricated using the discrete method ($N = 3$).

N	Grating	λ_t (nm)	$\Delta\lambda_t$ (nm)	λ_m (nm)	$\Delta\lambda_m$ (nm)	$\mathrm{Err}_{\mathrm{abs}}$ (%)	$\mathrm{Err}_{\mathrm{spacing}}$ (nm)
3	G1	650	-	663	-	2.00	-
	G2	680	30	685	22	0.74	8
	G3	710	30	711	26	0.14	4

4.3.4 Quadruple MSPG ($N = 4$)

The normalized reflectance spectra as a function of wavelength for a quadruple MSPG ($N = 4$) are presented in Figure 4.7, while the corresponding target and measured resonance wavelengths and associated errors are summarized in Table 4.4.

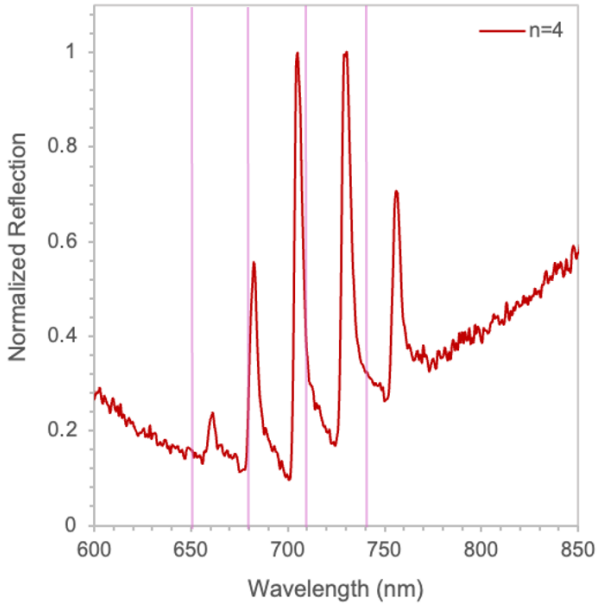

Figure 4.7 – Normalized reflectance spectra versus wavelength for a quadruple MSPG ($N = 4$) fabricated using the discrete method. The measured resonance wavelengths correspond to those reported in Table 4.4.

Table 4.4 – Target and measured resonance wavelengths for a quadruple MSPG fabricated using the discrete method ($N = 4$).

N	Grating	λ_t (nm)	$\Delta\lambda_t$ (nm)	λ_m (nm)	$\Delta\lambda_m$ (nm)	$\mathrm{Err}_{\mathrm{abs}}$ (%)	$\mathrm{Err}_{\mathrm{spacing}}$ (nm)
4	G1	650	-	661	-	1.69	-
	G2	680	30	682	21	0.29	9
	G3	710	30	705	23	0.70	7
	G4	740	30	730	25	1.35	5

It is worth nothing that an anomalous additional peak is observed at $\lambda_m = 756$ nm. This feature may have arisen from unintended mode coupling or fabrication non-uniformity that could have been introduced during the sequential grating superposition. This deviation represents the only occurrence of such an anomaly in the dataset and is thus treated as an outlier.

4.3.5 Quintuple MSPG ($N = 5$)

The normalized reflectance spectra as a function of wavelength for a quintuple MSPG ($N = 5$) are presented in Figure 4.8, while the corresponding target and measured resonance wavelengths and associated errors are summarized in Table 4.5.

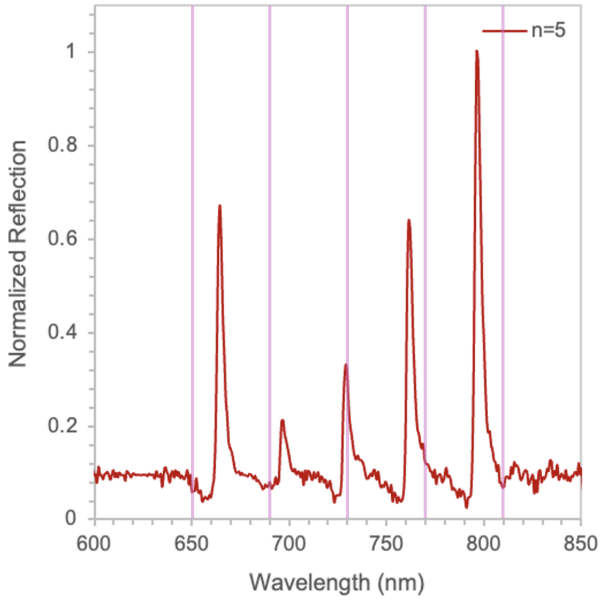

Figure 4.8 – Normalized reflectance spectra versus wavelength for a quintuple MSPG ($N = 5$) fabricated using the discrete method. The measured resonance wavelengths correspond to those reported in Table 4.5.

Table 4.5 – Target and measured resonance wavelengths for a quintuple MSPG fabricated using the discrete method ($N = 5$).

N	Grating	λ_t (nm)	$\Delta\lambda_t$ (nm)	λ_m (nm)	$\Delta\lambda_m$ (nm)	$\mathrm{Err}_{\mathrm{abs}}$ (%)	$\mathrm{Err}_{\mathrm{spacing}}$ (nm)
5	G1	650	-	664	-	2.15	-
	G2	690	40	696	32	0.87	8
	G3	730	40	729	33	0.14	7
	G4	770	40	761	32	1.17	8
	G5	810	40	796	35	1.73	5

4.3.6 Sextuple MSPG ($N = 6$)

The normalized reflectance spectra as a function of wavelength for a sextuple MSPG ($N = 6$) are presented in Figure 4.9, while the corresponding target and measured resonance wavelengths and associated errors are summarized in Table 4.6.

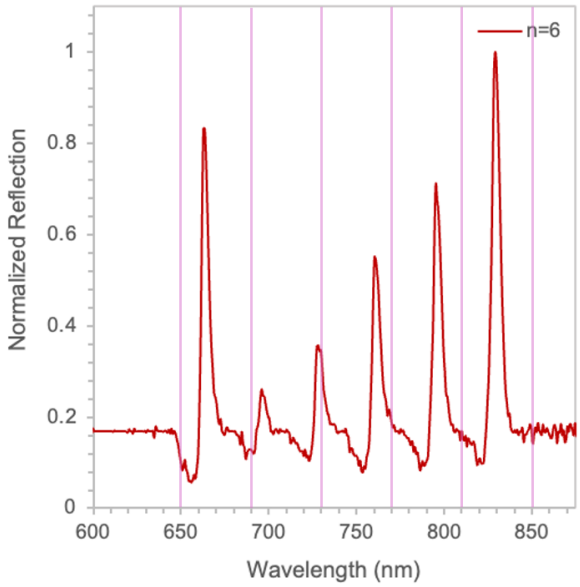

Figure 4.9 – Normalized reflectance spectra versus wavelength for a sextuple MSPG ($N = 6$) fabricated using the discrete method. The measured resonance wavelengths correspond to those reported in Table 4.6.

Table 4.6 – Target and measured resonance wavelengths for a sextuple MSPG fabricated using the discrete method ($N = 6$).

N	Grating	λ_t (nm)	$\Delta\lambda_t$ (nm)	λ_m (nm)	$\Delta\lambda_m$ (nm)	$\mathrm{Err}_{\mathrm{abs}}$ (%)	$\mathrm{Err}_{\mathrm{spacing}}$ (nm)
6	G1	650	-	663	-	2.00	-
	G2	690	40	697	34	1.01	6
	G3	730	40	728	31	0.27	9
	G4	770	40	760	32	1.30	8
	G5	810	40	795	35	1.85	5
	G6	850	40	830	35	2.35	5

4.3.7 Septuple MSPG ($N = 7$)

The normalized reflectance spectra as a function of wavelength for a septuple MSPG ($N = 7$) are presented in Figure 4.10, while the corresponding target and measured resonance wavelengths and associated errors are summarized in Table 4.7.

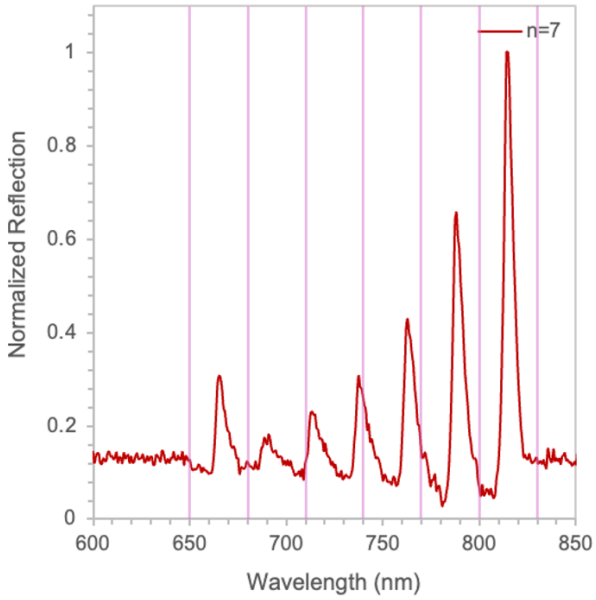

Figure 4.10 – Normalized reflectance spectra versus wavelength for a septuple MSPG ($N = 7$) fabricated using the discrete method. The measured resonance wavelengths correspond to those reported in Table 4.7.

Table 4.7 – Target and measured resonance wavelengths for a septuple MSPG fabricated using the discrete method ($N = 7$).

N	Grating	λ_t (nm)	$\Delta\lambda_t$ (nm)	λ_m (nm)	$\Delta\lambda_m$ (nm)	$\mathrm{Err}_{\mathrm{abs}}$ (%)	$\mathrm{Err}_{\mathrm{spacing}}$ (nm)
7	G1	650	-	665	-	2.31	-
	G2	680	30	689	24	1.32	6
	G3	710	30	712	23	0.28	7
	G4	740	30	737	25	0.41	5
	G5	770	30	763	26	0.91	4
	G6	800	30	788	25	1.50	5
	G7	830	30	814	26	1.93	4

4.3.8 Octuple MSPG ($N = 8$)

The normalized reflectance spectra as a function of wavelength for an octuple MSPG ($N = 8$) are presented in Figure 4.11, while the corresponding target and measured resonance wavelengths and associated errors are summarized in Table 4.8.

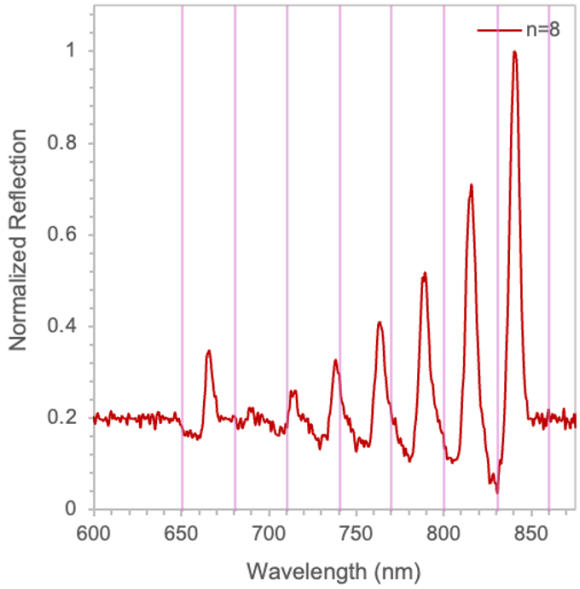

Figure 4.11 – Normalized reflectance spectra versus wavelength for an octuple MSPG ($N = 8$) fabricated using the discrete method. The measured resonance wavelengths correspond to those reported in Table 4.8.

Table 4.8 – Target and measured resonance wavelengths for an octuple MSPG fabricated using the discrete method ($N = 8$).

N	Grating	λ_t (nm)	$\Delta\lambda_t$ (nm)	λ_m (nm)	$\Delta\lambda_m$ (nm)	$\mathrm{Err}_{\mathrm{abs}}$ (%)	$\mathrm{Err}_{\mathrm{spacing}}$ (nm)
8	G1	650	-	664	-	2.15	-
	G2	680	30	691	27	1.62	3
	G3	710	30	713	22	0.42	8
	G4	740	30	738	25	0.27	5
	G5	770	30	765	27	0.65	3
	G6	800	30	788	23	1.50	7
	G7	830	30	816	28	1.69	2
	G8	860	30	840	24	2.33	6

4.3.9 Nonuple MSPG ($N = 9$)

The normalized reflectance spectra as a function of wavelength for a nonuple MSPG ($N = 9$) are presented in Figure 4.12, while the corresponding target and measured resonance wavelengths and associated errors are summarized in Table 4.9.

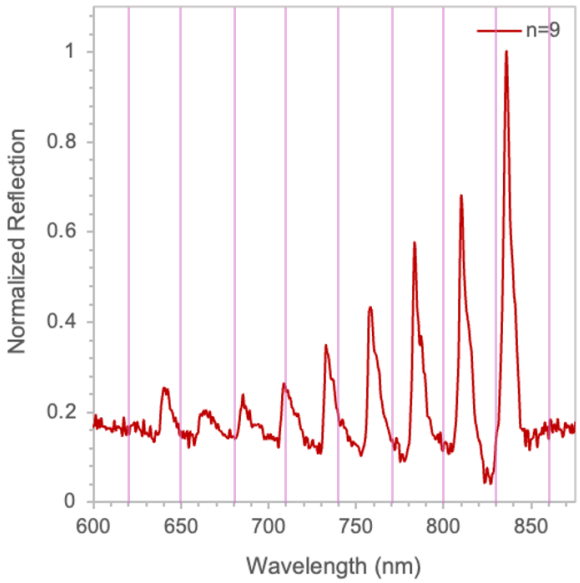

Figure 4.12 – Normalized reflectance spectra versus wavelength for a nonuple MSPG ($N = 9$) fabricated using the discrete method. The measured resonance wavelengths correspond to those reported in Table 4.9.

Table 4.9 – Target and measured resonance wavelengths for a nonuple MSPG fabricated using the discrete method ($N = 9$).

N	Grating	λ_t (nm)	$\Delta\lambda_t$ (nm)	λ_m (nm)	$\Delta\lambda_m$ (nm)	$\mathrm{Err}_{\mathrm{abs}}$ (%)	$\mathrm{Err}_{\mathrm{spacing}}$ (nm)
9	G1	620	-	642	-	3.55	-
	G2	650	30	664	22	2.15	8
	G3	680	30	685	21	0.74	9
	G4	710	30	710	25	0.00	5
	G5	740	30	733	23	0.95	7
	G6	770	30	758	25	1.56	5
	G7	800	30	783	25	2.13	5
	G8	830	30	810	27	2.41	3
	G9	860	30	836	26	2.79	4

4.3.10 Decuple MSPG ($N = 10$)

The normalized reflectance spectra as a function of wavelength for a decuple MSPG ($N = 10$) are presented in Figure 4.13, while the corresponding target and measured resonance wavelengths and associated errors are summarized in Table 4.10.

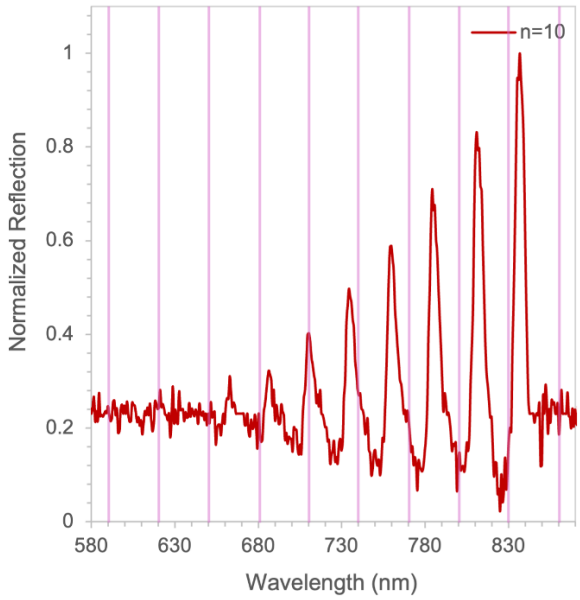

Figure 4.13 – Normalized reflectance spectra versus wavelength for a decuple MSPG ($N = 10$) fabricated using the discrete method. The measured resonance wavelengths correspond to those reported in Table 4.10.

Table 4.10 – Target and measured resonance wavelengths for a decuple MSPG fabricated using the discrete method ($N = 10$).

N	Grating	λ_t (nm)	$\Delta\lambda_t$ (nm)	λ_m (nm)	$\Delta\lambda_m$ (nm)	$\mathrm{Err}_{\mathrm{abs}}$ (%)	$\mathrm{Err}_{\mathrm{spacing}}$ (nm)
10	G1	590	-	595	-	0.85	-
	G2	620	30	619	24	0.16	6
	G3	650	30	663	44	2.00	14
	G4	680	30	687	24	1.03	6
	G5	710	30	710	23	0.00	7
	G6	740	30	735	25	0.68	5
	G7	770	30	759	24	1.43	6
	G8	800	30	784	25	2.00	5
	G9	830	30	810	26	2.41	4
	G10	860	30	836	26	2.79	4

The first two emission peaks of the decuple MSPG exhibit noticeably weaker intensities compared to other high order MSPGs as they are partially obscured by signal noise. As a result, the reflection peaks associated with gratings G1 and G2 are more difficult to identify with a high degree of confidence which explains the discrepancy between the target and measured wavelength spacing ($\Delta\lambda_m$ is 44 nm vs. 30 nm). This is likely due to the target wavelengths λ_t for G1 and G2, which

in comparison to the subsequent values are relatively low. As the number of gratings inscribed on top of one another reached $N = 10$, G1 and G2 may have been partially overwritten thus resulting in weakened intensities as presented on the graph.

4.3.11 Discussion

Based on the presented results, the following observations can be made. The absolute error (Err_{abs}) among all MSPGs varied between 0.14-3.55%, with an average value of 1.35%. This indicates that the discrete MSPG fabrication method was effective as it reproduced the target reflection wavelengths with a relatively small margin of error. Furthermore, the spacing among adjacent target and measured reflection peaks was generally smaller than expected, thus revealing a slight compression effect with the spacing error ($\text{Err}_{\text{spacing}}$) ranging between 2-14 nm, with an average value of $\sim$6 nm. By visually inspecting the graphs and interpreting the numerical results in the corresponding tables, the experimental results also reveal an interesting pattern. As the MSPG orders increase and reach the $N = 7$ to $N = 10$ range, shorter wavelength spectra (650–710 nm) tend to redshift and thus lie to the right of the expected values (larger spectral spacing between adjacent resonances), while longer wavelength spectra (710–860 nm) tend to blueshift and lie to the left of the expected values (smaller spectral spacing between adjacent resonances). For these MSPGs, the smallest absolute error occurred around the 710 nm wavelength, reaching as low as 0% ($\lambda_t = \lambda_m$). This indicates that the estimated effective refractive index of $n_{estimated} = 1.57$ used in Equation 3.2.3 to determine the designed grating pitches was most accurate near the centre of the spectral range, and that at this wavelength $n_{estimated} \approx n_{eff}$.

To further understand the mechanism of spectroscopic reflection peaks and their correlation to retroreflection, it is important to bridge critical concepts from the theory and experimental methodology sections. As the MSPG modulation depth increases through optimization, the diffraction efficiency improves as there is a more even distribution of energy into the allowed diffraction orders (in this case, $m = \pm 0, 1$). This enables more coupling into specific waveguiding modes, thus leading to more retroreflections of that particular mode into and out of the thin film, which directly correlates to a clear reflection peak in the spectroscopic measurements.

As discussed in Chapter 1, gratings act as couplers and filters of light, and as such can modify spectral signatures through manipulation of incident light, in this case to enhance reflection. This property of gratings can be exploited for both non-resonant (broadband) or resonant (narrowband) filtering, in which the spectrum of reflected or transmitted light is reduced as much as possible to create broad or sharp emission peaks, thus creating a distinct spectral fingerprint. The discrete MSPG method thus presents a unique combination of these two filtering techniques in which resonant (narrowband) filtering occurs across a broadband spectrum in the optical regime, meaning the reflection bandwidth is widened through the use of discrete resonance peaks, which is an underexplored area of research. By creating a multitude of spectral enhancements across the optical regime, MSPGs can be used to passively conceal spectral signatures by decreasing the visibility of precise wavelengths, which in turn increases the difficulty of detection. This has relevant applications to signature management in the context of optical engineering and photonics, as well as pan-domain military operations pertaining to stealth, remote sensing and general asset tracking including land vehicles, ships, aircraft and spacecraft.

4.4 MSPG Spectroscopy Data (Continuous Method)

The results of the second MSPG fabrication method, also referred to as the continuous method, will now be presented. As with the discrete process, this technique also aimed to achieve a broad-

band spectral response. By incrementally decreasing the spectral spacing between each set of discrete emission peaks, it was hypothesized that the resultant peaks would converge to form one broad peak across the range of corresponding target wavelength values. This would also accomplish the goal of widening the reflection bandwidth as each MSPG would retroreflect a cohesive bandwidth of incident light, thus broadening its respective spectral fingerprint and increasing the difficulty of detection. Interestingly, the opposite effect occurred. As MSPG orders increased, the convergence of the discrete peaks actually produced a narrowing effect, resulting in a compression of the measured wavelength range $\Delta\lambda_m$ in comparison to the target ranges $\Delta\lambda_t$. This will be explained in more detail in the discussion section after the results are presented.

The results for the continuous MSPGs are presented in the same way as the discrete method results. As a reminder, they are described as follows. For each continuous or converged MSPG, a graph of normalized reflectance ($\%R$) versus wavelength (λ) in nm is presented to demonstrate the recorded spectral response, however this time there are no vertical lines inserted in the graphs to represent the theoretical reflection wavelengths. Each graph has a corresponding table below it with the same eight parameters as presented in the discrete method results. The first column is n, representing the number of stacked gratings within an MSPG. Next is the grating number (G1, G2, G3, etc.), which represents the order of gratings in the PS 'stack'. Following this is the target wavelength λ_t, and separation distance between adjacent target wavelengths $\Delta\lambda_t$. The measured wavelength λ_m and separation distance between measured adjacent wavelengths $\Delta\lambda_m$ are then presented, followed by the absolute error Err_{abs} and relative spacing error $\text{Err}_{\text{spacing}}$.

4.4.1 Bi MSPG ($N = 2$)

The normalized reflectance spectra as a function of wavelength for a bi MSPG ($N = 2$) are presented in Figure 4.14, while the corresponding target and measured resonance wavelengths and associated errors are summarized in Table 4.11.

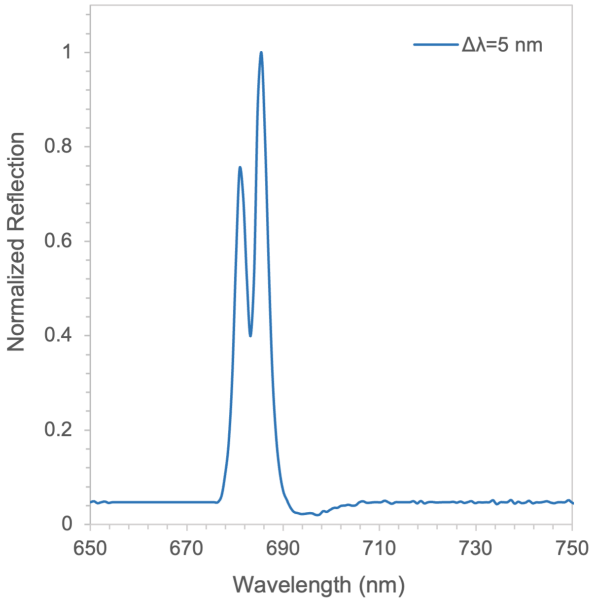

Figure 4.14 – Normalized reflectance spectra versus wavelength for a bi MSPG ($N = 2$) fabricated using the continuous method. The measured resonance wavelengths correspond to those reported in Table 4.11.

Table 4.11 – Target and measured resonance wavelengths for a bi MSPG fabricated using the continuous peak convergence method ($N = 2$).

N	Grating	λ_t (nm)	$\Delta\lambda_t$ (nm)	λ_m (nm)	$\Delta\lambda_m$ (nm)	Err_{abs} (%)	$\text{Err}_{\text{spacing}}$ (nm)
2	G1	650	-	681	-	4.77	-
	G2	655	5	685	4	4.58	1

4.4.2 Triple MSPG ($N = 3$)

The normalized reflectance spectra as a function of wavelength for a triple MSPG ($N = 3$) are presented in Figure 4.15, while the corresponding target and measured resonance wavelengths and associated errors are summarized in Table 4.12.

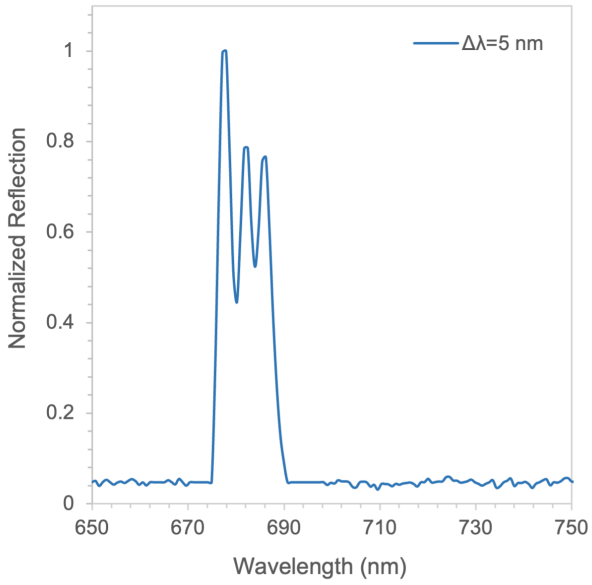

Figure 4.15 – Normalized reflectance spectra versus wavelength for a triple MSPG ($N = 3$) fabricated using the continuous method. The measured resonance wavelengths correspond to those reported in Table 4.12.

Table 4.12 – Target and measured resonance wavelengths for a triple MSPG fabricated using the continuous peak convergence method ($N = 3$).

N	Grating	λ_t (nm)	$\Delta\lambda_t$ (nm)	λ_m (nm)	$\Delta\lambda_m$ (nm)	Err_{abs} (%)	$\text{Err}_{\text{spacing}}$ (nm)
3	G1	650	-	677	-	4.15	-
	G2	655	5	681	4	3.97	1
	G3	660	5	685	4	3.79	1

4.4.3 Quadruple MSPG ($N = 4$)

The normalized reflectance spectra as a function of wavelength for a quadruple MSPG ($N = 4$) are presented in Figure 4.16, while the corresponding target and measured resonance wavelengths and associated errors are summarized in Table 4.13.

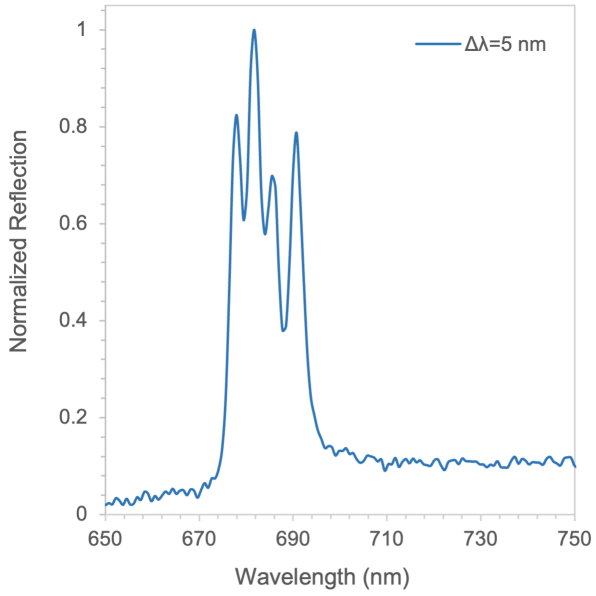

Figure 4.16 – Normalized reflectance spectra versus wavelength for a quadruple MSPG ($N = 4$) fabricated using the continuous method. The measured resonance wavelengths correspond to those reported in Table 4.13.

Table 4.13 – Target and measured resonance wavelengths for a quadruple MSPG fabricated using the continuous peak convergence method ($N = 4$).

N	Grating	λ_t (nm)	$\Delta\lambda_t$ (nm)	λ_m (nm)	$\Delta\lambda_m$ (nm)	Err_{abs} (%)	$\text{Err}_{\text{spacing}}$ (nm)
4	G1	650	-	678	-	4.31	-
	G2	655	5	682	4	4.12	1
	G3	660	5	685	3	3.79	2
	G4	665	5	691	6	3.91	1

4.4.4 Quintuple MSPG ($N = 5$)

The normalized reflectance spectra as a function of wavelength for a quintuple MSPG ($N = 5$) are presented in Figure 4.17, while the corresponding target and measured resonance wavelengths and associated errors are summarized in Table 4.14.

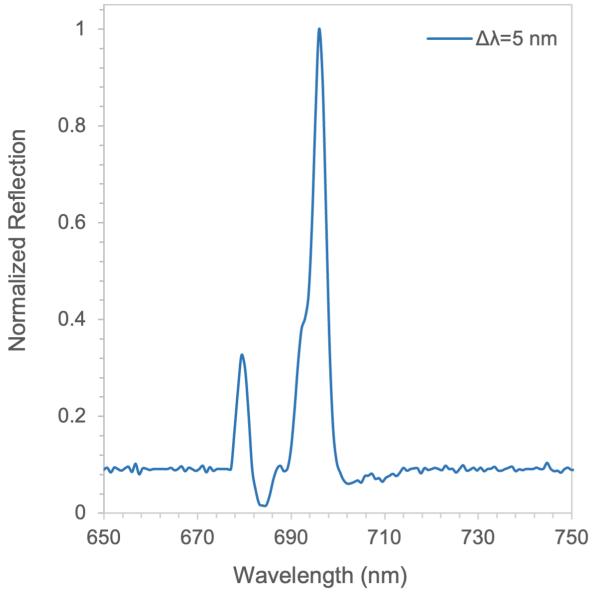

Figure 4.17 – Normalized reflectance spectra versus wavelength for a quintuple MSPG ($N = 5$) fabricated using the continuous method. The measured resonance wavelengths correspond to those reported in Table 4.14.

Table 4.14 – Target and measured resonance wavelengths for a quintuple MSPG fabricated using the continuous peak convergence method ($N = 5$).

N	Grating	λ_t (nm)	$\Delta\lambda_t$ (nm)	λ_m (nm)	$\Delta\lambda_m$ (nm)	$\mathrm{Err}_{\mathrm{abs}}$ (%)	$\mathrm{Err}_{\mathrm{spacing}}$ (nm)
5	G1	650	-	679	-	4.46	-
	G2	655	5	683	4	4.27	1
	G3	660	5	689	6	4.39	1
	G4	665	5	692	3	4.06	2
	G5	670	5	696	4	3.88	1

4.4.5 Sextuple MSPG ($N = 6$)

The normalized reflectance spectra as a function of wavelength for a sextuple MSPG ($N = 6$) are presented in Figure 4.18, while the corresponding target and measured resonance wavelengths and associated errors are summarized in Table 4.15.

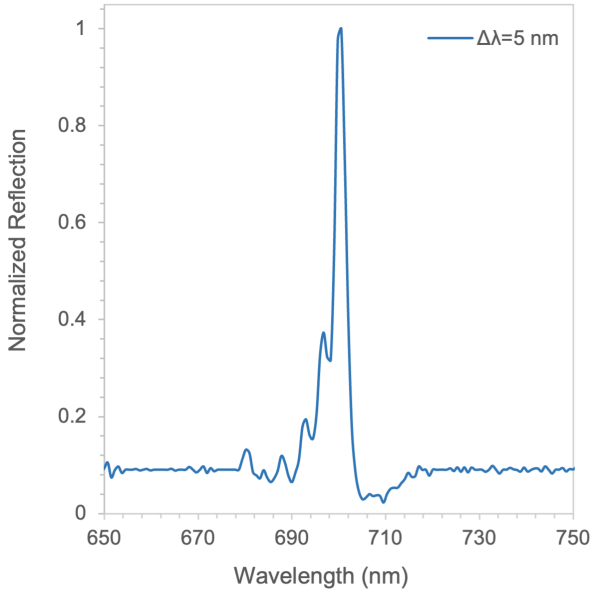

Figure 4.18 – Normalized reflectance spectra versus wavelength for a sextuple MSPG ($N = 6$) fabricated using the continuous method. The measured resonance wavelengths correspond to those reported in Table 4.15.

Table 4.15 – Target and measured resonance wavelengths for a sextuple MSPG fabricated using the continuous peak convergence method ($N = 6$).

N	Grating	λ_t (nm)	$\Delta\lambda_t$ (nm)	λ_m (nm)	$\Delta\lambda_m$ (nm)	$\mathrm{Err}_{\mathrm{abs}}$ (%)	$\mathrm{Err}_{\mathrm{spacing}}$ (nm)
6	G1	650	-	680	-	4.62	-
	G2	655	5	684	4	4.43	1
	G3	660	5	688	4	4.24	1
	G4	665	5	692	4	4.06	1
	G5	670	5	697	5	4.03	0
	G6	675	5	700	3	3.70	2

4.4.6 Septuple MSPG ($N = 7$)

The normalized reflectance spectra as a function of wavelength for a septuple MSPG ($N = 7$) are presented in Figure 4.19, while the corresponding target and measured resonance wavelengths and associated errors are summarized in Table 4.16.

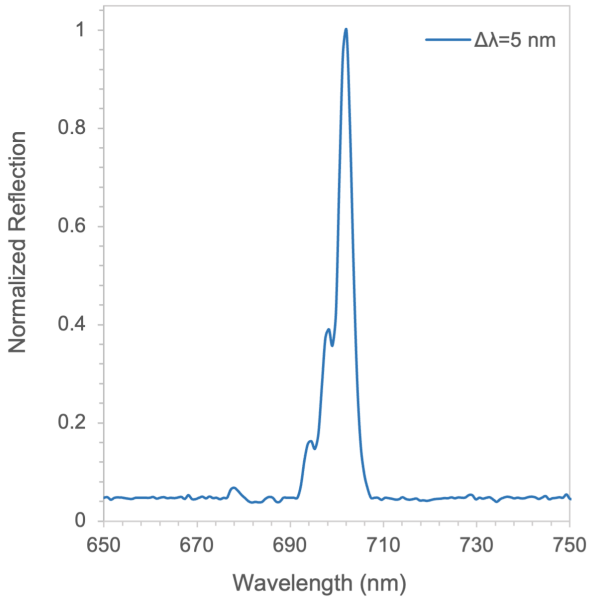

Figure 4.19 – Normalized reflectance spectra versus wavelength for a septuple MSPG ($N = 7$) fabricated using the continuous method. The measured resonance wavelengths correspond to those reported in Table 4.16.

Table 4.16 – Target and measured resonance wavelengths for a septuple MSPG fabricated using the continuous peak convergence method ($N = 7$).

N	Grating	λ_t (nm)	$\Delta\lambda_t$ (nm)	λ_m (nm)	$\Delta\lambda_m$ (nm)	$\mathrm{Err}_{\mathrm{abs}}$ (%)	$\mathrm{Err}_{\mathrm{spacing}}$ (nm)
7	G1	650	-	679	-	4.46	-
	G2	655	5	684	5	4.43	0
	G3	660	5	685	1	3.79	4
	G4	665	5	690	5	3.76	0
	G5	670	5	695	5	3.73	0
	G6	675	5	697	2	3.26	3
	G7	680	5	702	5	3.24	0

4.4.7 Octuple MSPG ($N = 8$)

The normalized reflectance spectra as a function of wavelength for a octuple MSPG ($N = 8$) are presented in Figure 4.20, while the corresponding target and measured resonance wavelengths and associated errors are summarized in Table 4.17.

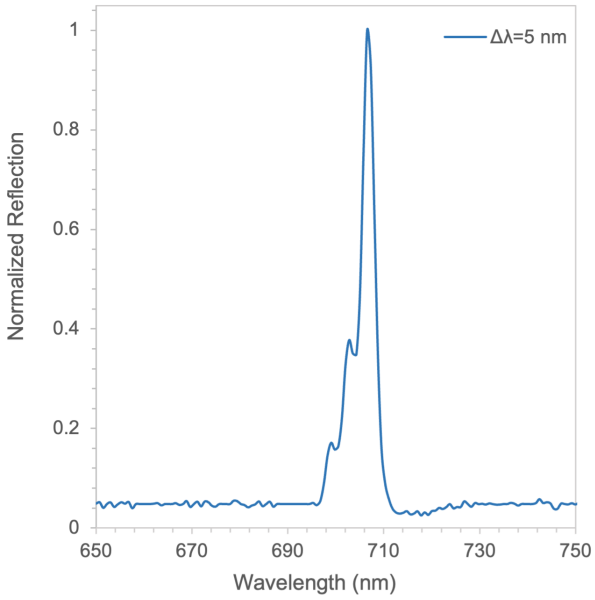

Figure 4.20 – Normalized reflectance spectra versus wavelength for an octuple MSPG ($N = 8$) fabricated using the continuous method. The measured resonance wavelengths correspond to those reported in Table 4.17.

Table 4.17 – Target and measured resonance wavelengths for an octuple MSPG fabricated using the continuous peak convergence method ($N = 8$).

N	Grating	λ_t (nm)	$\Delta\lambda_t$ (nm)	λ_m (nm)	$\Delta\lambda_m$ (nm)	$\mathrm{Err}_{\mathrm{abs}}$ (%)	$\mathrm{Err}_{\mathrm{spacing}}$ (nm)
8	G1	650	-	679	-	4.46	-
	G2	655	5	684	5	4.43	0
	G3	660	5	686	2	3.94	3
	G4	665	5	691	5	3.91	0
	G5	670	5	695	4	3.73	1
	G6	675	5	699	4	3.56	1
	G7	680	5	703	4	3.38	1
	G8	685	5	707	4	3.21	1

4.4.8 Nonuple MSPG ($N = 9$)

The normalized reflectance spectra as a function of wavelength for a nonuple MSPG ($N = 9$) are presented in Figure 4.21, while the corresponding target and measured resonance wavelengths and associated errors are summarized in Table 4.18.

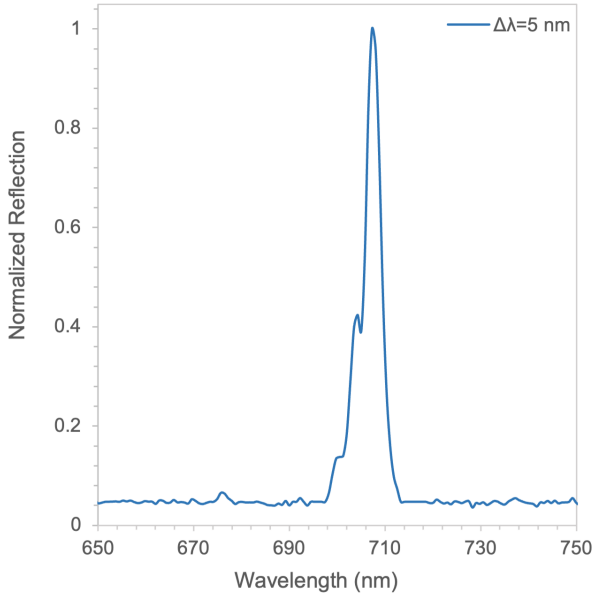

Figure 4.21 – Normalized reflectance spectra versus wavelength for a nonuple MSPG ($N = 9$) fabricated using the continuous method. The measured resonance wavelengths correspond to those reported in Table 4.18.

Table 4.18 – Target and measured resonance wavelengths for a nonuple MSPG fabricated using the continuous peak convergence method ($N = 9$).

N	Grating	λ_t (nm)	$\Delta\lambda_t$ (nm)	λ_m (nm)	$\Delta\lambda_m$ (nm)	$\mathrm{Err}_{\mathrm{abs}}$ (%)	$\mathrm{Err}_{\mathrm{spacing}}$ (nm)
9	G1	650	-	676	-	4.00	-
	G2	655	5	679	3	3.66	2
	G3	660	5	683	4	3.48	1
	G4	665	5	688	5	3.46	0
	G5	670	5	692	4	3.28	1
	G6	675	5	697	5	3.26	0
	G7	680	5	701	4	3.09	1
	G8	685	5	704	3	2.77	2
	G9	690	5	707	3	2.46	2

4.4.9 Decuple MSPG ($N = 10$)

The normalized reflectance spectra as a function of wavelength for a decuple MSPG ($N = 10$) are presented in Figure 4.22, while the corresponding target and measured resonance wavelengths and associated errors are summarized in Table 4.19.

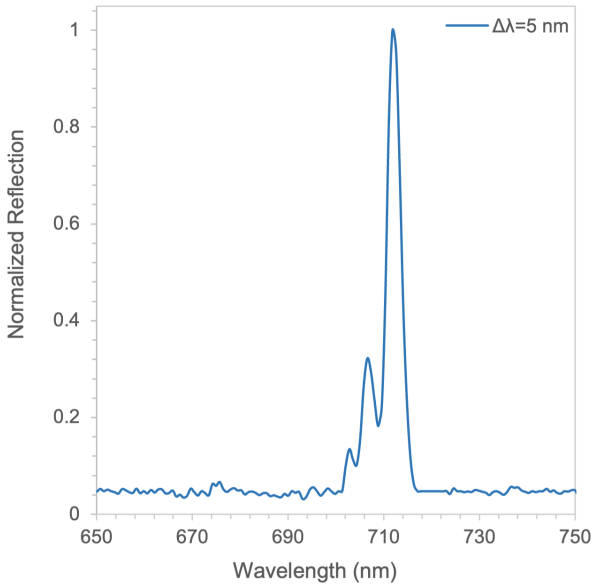

Figure 4.22 – Normalized reflectance spectra versus wavelength for a decuple MSPG ($N = 10$) fabricated using the continuous method. The measured resonance wavelengths correspond to those reported in Table 4.19.

Table 4.19 – Target and measured resonance wavelengths for a decuple MSPG fabricated using the continuous peak convergence method ($N = 10$).

N	Grating	λ_t (nm)	$\Delta\lambda_t$ (nm)	λ_m (nm)	$\Delta\lambda_m$ (nm)	$\mathrm{Err}_{\mathrm{abs}}$ (%)	$\mathrm{Err}_{\mathrm{spacing}}$ (nm)
10	G1	650	-	676	-	4.00	-
	G2	655	5	679	3	3.66	2
	G3	660	5	682	3	3.33	2
	G4	665	5	687	5	3.31	0
	G5	670	5	692	5	3.28	0
	G6	675	5	695	3	2.96	2
	G7	680	5	698	3	2.65	2
	G8	685	5	703	5	2.63	0
	G9	690	5	707	4	2.46	1
	G10	695	5	712	5	2.45	0

4.4.10 Discussion

According to the above results, several key observations can be made regarding the continuous MSPG fabrication method. The absolute error (Err_{abs}) among all continuous MSPGs varied between 2.45-4.77%, with an average value of ∼3.72%. Comparatively, the average absolute error in the discrete method was ∼1.35%, indicating that the continuous peak convergence approach reproduces target reflection wavelengths with less accuracy. Just as in the discrete method, Err_{abs} decreased with increasing MSPG orders and as the number of gratings within each MSPG increased. The lowest value of Err_{abs} was 2.45% and occured at the measured wavelength value $\lambda_m = 712$ nm. This strongly aligns with the observations in the discrete method, which also saw the lowest Err_{abs} values occurring when $\lambda_m \simeq 710$ nm.

In all continuous method results, the measured spacing among individual resonance wavelengths $\Delta\lambda_m$ between converging peaks were larger than the target wavelengths $\Delta\lambda_t$ by a factor of ∼22-30 nm, with this number generally decreasing with increasing MSPG orders. Combined emission peaks for all MSPGs thus experienced a global systematic redshift toward longer wavelengths relative to their design values. Despite this overall offset, the relative spacing between adjacent measured resonances generally remained close to the intended target spacing of 5 nm. This is indicated through the spacing error ($\text{Err}_{\text{spacing}}$), which ranged between 0-4 nm with an average value of ∼1.09 nm. This suggests that the continuous method preserved the relative ordering and local spacing of adjacent resonances reasonably well, even though the full set of peaks shifted to the right of the target wavelength ranges.

As previously mentioned, the continuous method did not produce the anticipated broadband spectral convergence as expected. The initial hypothesis proposed that incrementally reducing the target spacing between adjacent gratings would cause the discrete resonances to merge into a single broad reflection band across the range of target reflection wavelengths. Experimentally, the opposite trend was observed as the MSPG order increased. The measured resonance ranges became slightly compressed relative to the target wavelength span, and the emission peaks generally converged towards a singular sharp resonance rather than a continuous broadband feature. Although the inter-peak spacing values for these MSPGs were reproduced with relatively small margins of error, the overall reflection bandwidth did not broaden to the intended scale. It is worth noting that while the converged peaks compressed and tapered vertically towards their tips, the bandwidth of their bases actually remained relatively wide in comparison (∼15-20 nm), often reduced to approximately half of the target bandwidth. Given this, the results still achieved a continuous reflection bandwidth albeit with a relatively narrowband effect. As mentioned in Chapter 1, typically discrete resonances would be exploited to create a narrowband effect, while in this case a continuous or non-resonant spectral enhancement has been demonstrated to create a narrowband response.

Another noteworthy observation is that for higher order MSPGs, the tips of the converged peaks generally aligned with the expected target wavelength of the last inscribed grating, indicating that the final grating inscription within each MSPG likely exerted the strongest influence on the measured resonance position within the superimposed structure. This was especially noticeable in the $N = 5$ to $N = 10$ MSPGs, and is interesting as the gratings within these metasurfaces were written with identical exposure times, with the exception of the first (G1). In these particular MSPGs, each subsequent grating (G2-G10) was exposed for 60 seconds, suggesting that exposure time alone did not significantly affect the shape of the peak convergence. Instead, this behaviour could have been influenced by other factors such as changes in effective refractive index of the azobenzene film resulting from repeated laser exposure, or inter-grating interference due to the close spacing of the superimposed gratings.

In contrast, lower order MSPGs ($N = 2$ to $N = 4$) did not experience this same effect. Instead,

individual peaks within each MSPG had relatively similar depths and did not converge towards the last written grating. The merging of these peaks also appeared to produce more of a broadband result in comparison to the higher order MSPGs ($N = 5$ to $N = 10$). This could in part be due to the two different exposure time processes used for these sets of MSPGs as described in Chapter 3 (recall the V1 and V2 methods). Future research could include further refining the time optimization methods such that the continuous broadband response resembles its target wavelength range even more closely.

Despite the unexpected results, the continuous MSPG method remains significant as it demonstrates that closely spaced superimposed gratings can be used to engineer compact resonant spectral responses which are relevant to narrowband spectral filtering applications.

4.5 Spectral Validation via AFM FFT Analysis

While the presented results provide a reliable characterization of the optical response, further validation can be achieved by cross-correlating the discrete MSPG spectroscopic data with atomic force microscope (AFM) measurements using Fast Fourier Transform (FFT) analysis. The FFT provides a frequency-domain representation of the surface profile, where the magnitude of each peak reflects the relative contribution of a given spatial periodicity. FFT techniques can thus be used to mathematically confirm that the observed reflection peaks originate from the physically inscribed MSPGs, and that their corresponding periodicities correlate to the design grating pitch values. Although the proprietary AFM software (Nanoscope Analysis) has a built-in FFT function, it is limited by the scan resolution and only allows the detection of one periodicity per MSPG. This issue was addressed with an in-house custom FFT analysis code written in Python, which utilizes AFM data to enhance peak detection and resolution capabilities beyond that of the Nanoscope Analysis software by applying a clustered probability algorithm that can characterize the periodicities of multiple peaks with closely spaced frequencies.

Representative FFT results will now be presented for selected MSPG orders to illustrate the proof of concept of the FFT analysis and highlight the evolution of spatial frequency components with increasing MSPG orders N. As a baseline reference, the results for a single grating ($N = 1$) is shown first in Figure C.1 below. A single dominant peak is observed at approximately 410 nm, which is close to the designed grating pitch of 414 nm.

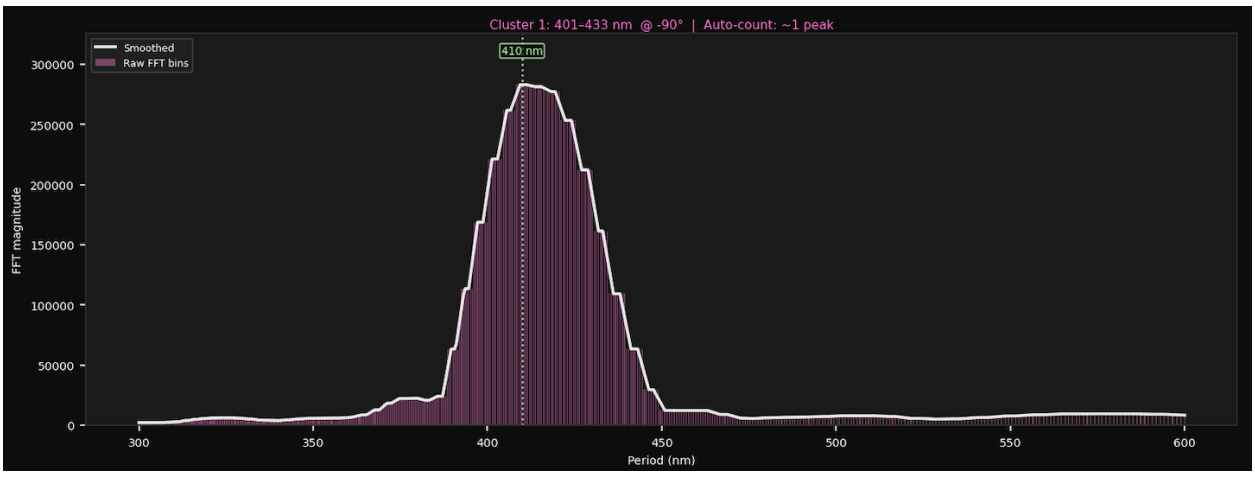

Figure 4.23 – FFT analysis of a single grating ($N = 1$) as a baseline reference.

As additional gratings are superimposed, multiple distinct peaks emerge within the FFT spectrum. For example, the triple MSPG ($N = 3$) below exhibits three clearly resolved peaks at approximately 411 nm, 429 nm, and 449 nm, corresponding closely to the expected grating pitches of 414 nm, 433 nm and 452 nm.

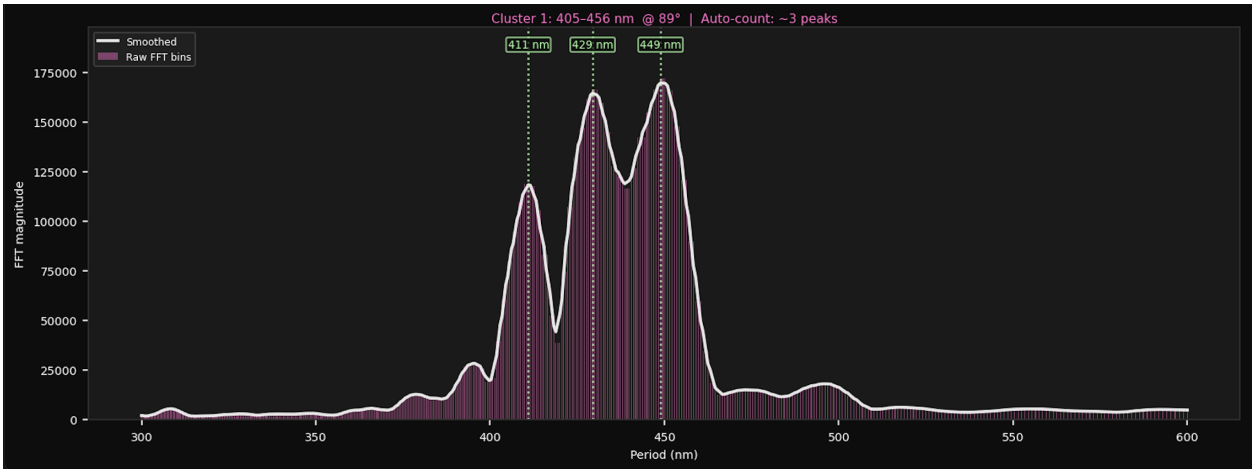

Figure 4.24 – FFT analysis of a triple MSPG ($N = 3$) showing multiple spatial frequency components.

Similarly, higher-order structures such as the sextuple MSPG ($N = 6$) show an increasing number of identifiable peaks, in this example exhibiting six distinct spatial frequency components of 411 nm, 438 nm, 462 nm, 487 nm, 512 nm, and 537 nm. These results also closely correlate to the respective design grating pitches of 414 nm, 440 nm, 465 nm, 490 nm, 516 nm, and 541 nm.

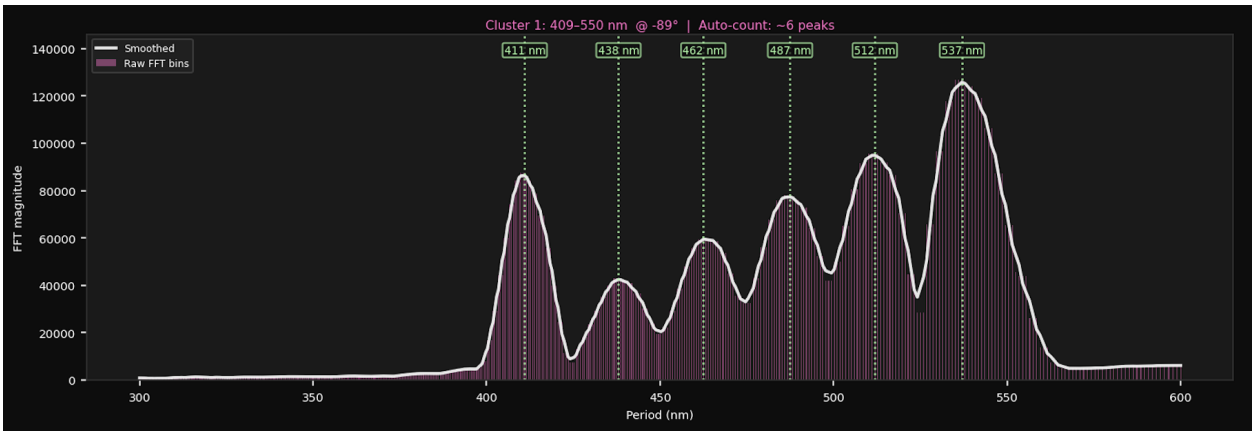

Figure 4.25 – FFT analysis of a sextuple MSPG ($N = 6$) showing multiple spatial frequency components.

In addition to the spectroscopy data presented earlier, these FFT results further confirm that multiple gratings are successfully inscribed and retained within the MSPG structures, with each individual grating within the parallel-superimposed 'stack' contributing a unique spatial frequency component. In addition to the grating pitches, the relative amplitudes of the FFT peaks were observed to qualitatively correlate with those of their corresponding spectroscopic reflection peaks. In other words, stronger FFT components aligned with higher-intensity reflection peaks and weaker

signals with lower-intensity peaks. As such, this FFT analysis further supports the direct relationship between grating modulation depth and optical response. Complete FFT datasets for all samples ($N = 1$ to $N = 10$) are provided in Appendix C.

Chapter 5

Conclusion

5.1 Summary

This study investigated the use of multi-superimposed parallel gratings (MSPGs) as a means of passive spectral enhancement to selectively widen the reflection bandwidth in the optical regime. To achieve this goal, two distinct fabrication approaches were explored. The first is referred to as the discrete method, in which multiple gratings with relatively large spectral spacing between corresponding target reflection peaks were sequentially superimposed to create distinct spectral responses across a wide bandwidth. The second is known as the continuous method, which consisted of incrementally reducing the spacing between adjacent discrete gratings in an attempt to converge them into a singular peak, thus generating a broadband reflection emission.

The experimental results demonstrate that both MSPG methods are a viable mechanism for selectively modifying optical spectral responses through grating superposition. In the discrete fabrication method, the target reflection wavelengths were reproduced with relatively high accuracy, with an average absolute error of approximately 1.35%. Although a slight compression of inter-peak spacing was observed, the discrete MSPGs successfully produced multiple distinct resonant reflection peaks across the optical spectrum ranging from ∼590–860 nm. These results demonstrate that the superposition of multiple parallel gratings can be used to generate broadband spectral enhancement through the distribution of multiple narrow resonances across a wide wavelength range. This behaviour is particularly noteworthy as broadband spectral responses are typically associated with non-resonant effects, whereas in this case the broadband effect is achieved through the deliberate superposition of multiple resonant grating responses. This concept can be implemented across many domains including biomimicry and military stealth applications. The distribution of distinct spectral features across a wide wavelength range can conceal or camouflage an object's true spectral signature as it blends into the spectroscopic background, effectively creating an artificial colour. As such, the discrete MSPG method represents a unique and novel approach to broadband resonant spectral engineering, thus pioneering a new research avenue for azobenzene-coated parallel-superimposed SRGs.

In contrast, the continuous fabrication method produced a slightly different spectral behavior than originally hypothesized. Rather than merging into a single broadband reflection emission, the converging peaks exhibited a global redshift relative to the target wavelengths, with an average absolute error of approximately 3.72%. Despite this systematic offset, the relative spacing between adjacent resonances remained close to the intended 5 nm design interval, indicating that the relative target spacing among spectral resonances was preserved. As the MSPG order increased, the converged peaks tended to compress and taper toward a singular dominant resonance rather than

forming a broad continuous reflection band. This result suggests that factors such as cumulative optical interactions between closely spaced gratings, as well as changes in the effective refractive index of the azobenzene film due to repeated exposure may influence the resultant spectral response. Although the intended broadband result was not achieved as expected, the results instead produced a narrowband filtering effect which is useful to a variety of photonics applications requiring wavelength isolation, such as astronomical and biomedical optical imagery, remote sensing and asset tracking.

The spectroscopic results were then validated via AFM FFT analysis for increased reliability in which the individual spatial frequency components within each discrete MSPG were clearly identified. These results demonstrated strong correlation between the designed grating pitches and the resultant FFT peaks, thereby confirming mathematically that the spectroscopic features observed in the results are directly linked to the inscribed periodicities.

The work in this thesis ultimately achieved the goal it set out to, however there remain several challenges and limitations that currently restrict the full potential of MSPG-based spectral signature engineering. While the overall experimental results showed little deviation from the theoretical design, several discrepancies between the target and measured resonance wavelengths were observed. In particular, systematic deviations in actual resonance positions and the spacing between adjacent resonances were present, especially for lower-order MSPGs. These differences are likely due to a combination of several factors, including estimations in the effective refractive index used during pitch calculations, fabrication tolerances in the grating pitch and depth, and perturbations arising from these factors such as the cumulative superposition of multiple gratings. From a design perspective, the current MSPG structures were limited to normal incidence ($\theta_i = 0°$) for the purpose of simplicity and proof of concept, whereas practical applications would likely require angular independence and retroreflection across a range of incident angles. Furthermore, fabrication constraints led to non-uniform modulation depths among superimposed gratings, which contribute to variations in peak intensity and spectral distortion.

Finally, in the context of optical signature management applications on the macro scale, such as military stealth, scaling the MSPG fabrication process to produce large-area arrays or mosaics would be both difficult and impractical with the current methodology. Fully integrating these metasurfaces onto aircraft or spacecraft would require hundreds or even thousands of precisely manufactured MSPGs, which would be excessively laborious and difficult to implement with the present fabrication technology. This impedes the ability to test these devices in realistic operational environments, thus limiting the current scope of MSPG applications to relatively small scales.

5.2 Future Work

To further expand upon the research conducted in this study, dedicated effort should be placed toward optimizing fabrication parameters such as exposure time, grating pitch, and azobenzene effective refractive index. This will be useful in achieving more uniform grating modulation depths, and likely offer better control of the spectral positioning and convergence behaviour of the MSPGs.

Additionally, work can be done to extend MSPG orders beyond $N = 10$ to further expand the enhancement bandwidth. Although there is no theoretical limit to the number of parallel-superimposed gratings within an MSPG, the photodynamic nature of azobenzene would eventually inhibit the observation of discrete peaks as N increases, because recently inscribed gratings would likely overwrite initially inscribed gratings. This effect was observed during the experimental process of this work and was corrected with rigorous optimization. Furthermore, as N increases, the initial gratings tend to produce weaker reflection peaks and blend with spectroscopic noise in the

visible regime. MSPG-enabled reflection enhancements should be designed with this in mind, also considering sensor detection limits and post-processing to reduce signal noise as much as possible by increasing the spectral contrast.

From a data analysis perspective, developing more robust spectral processing models to address imperfections in the baseline correction methods and refining the current FFT-based analysis process would also be beneficial. MSPG designs should be expanded to support both angle-dependent and independent behaviour, and retroreflection at multiple incident angles should be investigated in the context of surface plasmon resonance (SPR) in addition to guided-mode coupling.

Furthermore, MSPG transparency should be sought by transferring the gratings onto a transparent epoxy layer. This preserves the MSPG metasurface and its optical properties while removing the azobenzene layer, which is sensitive to specific changes in temperature and light. This step would enhance MSPG durability in harsh environments, thus enabling their implementation in operational settings with varying conditions, from terrestrial to space-based applications. The effect of epoxy thickness on guided-mode coupling and SPR should also be investigated, as it may influence the number of supported modes and overall spectral response. Finally, effort should be placed towards improving the efficiency and scalability of the discrete and continuous MSPG fabrication methods to enable implementation onto larger surface areas to increase the feasibility of macro-scale, operational applications.

Bibliography

[1] S. R. Wilk, *Light—as a Feather*, 1st ed. Oxford University Press, Mar. 2021, pp. 40–42.

[2] F. Hopkinson and D. Rittenhouse, "An Optical Problem, Proposed by Mr. Hopkinson, and Solved by Mr. Rittenhouse," *Transactions of the American Philosophical Society*, vol. 2, p. 201, 1786.

[3] G. W. Stroke, "Diffraction Gratings," in *Optische Instrumente*, S. Flügge and S. Flügge, Eds. Berlin, Heidelberg: Springer, 1967, vol. 5, pp. 426–754.

[4] Joseph von Fraunhofer, "Neue Modifikation des Lichtes durch gegenseitige Einwirkung und Beugung der Strahlen, und Gesetze derselben," *Denkschriften der Königlichen Akademie der Wissenschaften zu München*, vol. 8, pp. 3–76, 1821.

[5] M. Born and E. Wolf, *Principles of Optics: Electromagnetic Theory of Propagation, Interference and Diffraction of Light*, 7th ed. Cambridge, UK: Cambridge University Press, 2017.

[6] Christopher A. Palmer, *Diffraction Grating Handbook*, 8th ed. MKS Instruments (Richardson Gratings), Mar. 2020.

[7] R. A. Serway, J. W. Jewett, and V. Peroomian, *Physics for Scientists and Engineers with Modern Physics*, 9th ed. Boston, MA: Brooks/Cole, 2014.

[8] E. G. Loewen and E. Popov, *Diffraction Gratings and Applications*, 1st ed. New York, NY: Marcel Dekker, 1997.

[9] E. Hecht, *Optics*, 5th ed. Boston, MA: Pearson, 2017.

[10] S. Lee, "Holographic Recording Versus Holographic Lithography," *Current Optics and Photonics*, vol. 7, no. 6, pp. 638–654, Dec. 2023.

[11] P. Rochon, E. Batalla, and A. Natansohn, "Optically induced surface gratings on azoaromatic polymer films," *Applied Physics Letters*, vol. 66, no. 2, pp. 136–138, Jan. 1995.

[12] A. Natansohn and P. Rochon, "Photoinduced Motions in Azo-Containing Polymers," *Chemical Reviews*, vol. 102, no. 11, pp. 4139–4176, Nov. 2002.

[13] Su-no-G, "Isomerization of azobenzene," 2007.

[14] G. R. Harrison, "The Production of Diffraction Gratings I. Development of the Ruling Art," *Journal of the Optical Society of America*, vol. 39, no. 6, p. 413, Jun. 1949.

[15] K. Okamoto, *Fundamentals of Optical Waveguides*, 3rd ed. Academic Press, 2022.

[16] K. Yeow You, Ed., *Emerging Waveguide Technology*. IntechOpen, 2018.

[17] R. J. Stockermans and P. L. Rochon, "Narrow-band resonant grating waveguide filters constructed with azobenzene polymers," *Applied Optics*, vol. 38, no. 17, p. 3714, Jun. 1999.

[18] J. Qi, C. Li, Y. Xia, B. Fang, Z. Hong, L. Chen, and X. Jing, "Research progress of biomolecular detection based on metasurfaces," *Infrared Physics & Technology*, vol. 136, p. 105111, Jan. 2024.

[19] C. Li, P. Yu, Y. Huang, Q. Zhou, J. Wu, Z. Li, X. Tong, Q. Wen, H.-C. Kuo, and Z. M. Wang, "Dielectric metasurfaces: From wavefront shaping to quantum platforms," *Progress in Surface Science*, vol. 95, no. 2, p. 100584, May 2020.

[20] S. Zhang, C. L. Wong, S. Zeng, R. Bi, K. Tai, K. Dholakia, and M. Olivo, "Metasurfaces for biomedical applications: Imaging and sensing from a nanophotonics perspective," *Nanophotonics*, vol. 10, no. 1, pp. 259–293, Dec. 2020.

[21] D. Schurig, J. J. Mock, B. J. Justice, S. A. Cummer, J. B. Pendry, A. F. Starr, and D. R. Smith, "Metamaterial Electromagnetic Cloak at Microwave Frequencies," *Science*, vol. 314, no. 5801, pp. 977–980, Nov. 2006.

[22] B. Orazbayev, N. M. Estakhri, M. Beruete, and A. Alu, "Metasurface-based ultrathin carpet cloak," in *2016 10th European Conference on Antennas and Propagation (EuCAP)*. Davos, Switzerland: IEEE, Apr. 2016, pp. 1–3.

[23] K. Iwaszczuk, A. C. Strikwerda, K. Fan, X. Zhang, R. D. Averitt, and P. U. Jepsen, "Flexible metamaterial absorbers for stealth applications at terahertz frequencies," *Optics Express*, vol. 20, no. 1, p. 635, Jan. 2012.

[24] K. B. Alici and E. Özbay, "Radiation properties of a split ring resonator and monopole composite," *physica status solidi (b)*, vol. 244, no. 4, pp. 1192–1196, Apr. 2007.

[25] A. Li, S. Singh, and D. Sievenpiper, "Metasurfaces and their applications," *Nanophotonics*, vol. 7, no. 6, pp. 989–1011, Jun. 2018.

[26] S. Enoch, G. Tayeb, P. Sabouroux, N. Guérin, and P. Vincent, "A Metamaterial for Directive Emission," *Physical Review Letters*, vol. 89, no. 21, p. 213902, Nov. 2002.

[27] A. Zettel, Y. Bdour, and R. G. Sabat, "Angle-resolved polarization control of surface plasmon resonance in superimposed metallic gratings," *Journal of Physics D: Applied Physics*, vol. 59, no. 1, p. 015111, Jan. 2026.

[28] S. Bokhari, Y. Bdour, and R. G. Sabat, "Fabrication and Plasmonic Characterization of Metasurfaces Patterned via Tunable Pyramidal Interference Lithography," *Micromachines*, vol. 17, no. 1, p. 104, Jan. 2026.

[29] A. J. El-Helou, Y. Liu, C. Chen, F. Wang, H. Altug, P. J. Reece, and Y. Zhu, "Optical Metasurfaces for the Next-Generation Biosensing and Bioimaging," *Laser & Photonics Reviews*, vol. 19, no. 10, p. 2401715, May 2025.

[30] S. Sasidevi, S. Kumarganesh, S. Saranya, B. Thiyaneswaran, K. V. M. Shree, K. Martin Sagayam, B. K. Pandey, and D. Pandey, "Design of Surface Plasmon Resonance (SPR) Sensors for Highly Sensitive Biomolecular Detection in Cancer Diagnostics," *Plasmonics*, vol. 20, no. 2, pp. 677–689, May 2024.

[31] W. Yang, M. Jiang, S. Jiang, L. Du, Y. Cheng, P. Li, and C. Wang, "Design and fabrication of Gr/Ag-coated tilted grating sensor for ultra-sensitive detection of DNA hybridization," *Sensors and Actuators B: Chemical*, vol. 359, p. 131587, May 2022.

[32] A. Peterson, "Label-free imaging of cells and their extracellular matrix by SPR imaging," National Institute of Standards and Technology, Tech. Rep., Jun. 2025.

[33] T. Stav, A. Faerman, E. Maguid, D. Oren, V. Kleiner, E. Hasman, and M. Segev, "Quantum entanglement of the spin and orbital angular momentum of photons using metamaterials," *Science*, vol. 361, no. 6407, pp. 1101–1104, Sep. 2018.

[34] K. Wang, J. G. Titchener, S. S. Kruk, L. Xu, H.-P. Chung, M. Parry, I. I. Kravchenko, Y.-H. Chen, A. S. Solntsev, Y. S. Kivshar, D. N. Neshev, and A. A. Sukhorukov, "Quantum metasurface for multiphoton interference and state reconstruction," *Science*, vol. 361, no. 6407, pp. 1104–1108, Sep. 2018.

[35] M. Dollar, Y. Bdour, P. Rochon, and R. G. Sabat, "Surface Plasmon Mediated Angular and Wavelength Tunable Retroreflectors Using Parallel-Superimposed Surface Relief Bi-Gratings," *Applied Sciences*, vol. 15, no. 1, p. 339, Jan. 2025.

[36] T. Antonakakis, F. I. Baida, A. Belkhir, K. Cherednichenko, S. Cooper, R. Craster, G. Demésy, J. Desanto, G. Granet, B. Gralak, S. Guenneau, D. Maystre, A. Nicolet, B. Stout, F. Zolla, B. Vial, and E. Popov, *Gratings: Theory and Numeric Applications*, 1st ed. Presses Universitaire de Provence (PUP), 2012.

[37] D. Sobral, I. Smail, P. N. Best, J. E. Geach, Y. Matsuda, J. P. Stott, M. Cirasuolo, and J. Kurk, "A large Hα survey at z = 2.23, 1.47, 0.84 and 0.40: The 11 Gyr evolution of star-forming galaxies from HiZELS," *Monthly Notices of the Royal Astronomical Society*, vol. 428, no. 2, pp. 1128–1146, Jan. 2013.

[38] F. L. Pedrotti and L. S. Pedrotti, *Introduction to Optics*, 3rd ed. Cambridge University Press, Dec. 2017.

[39] D. J. Griffiths, *Introduction to Electrodynamics*, 3rd ed. Upper Saddle River, NJ: Prentice Hall, 1999.

[40] S. Ling, J. Sanny, and W. Moebs, "University physics. Volume 2." Houston: OpenStax, 2021.

[41] E. K. Bailey, "Surface Plasmon Polariton Bandwidth Increase Using Chirped-Pitch Linear Diffraction Gratings Fabricated On Azobenzene Thin Films," Master's thesis, Royal Military College of Canada, 2017.

[42] Y. Mikhyeyev, "Surface Plasmon Microscopy of Inhomogeneous Aqueous Mixtures," Master's thesis, Royal Military College of Canada, 2019.

[43] J. W. Goodman, *Introduction to Fourier Optics*, 4th ed. New York: W.H. Freeman, Macmillan Learning, 2017.

[44] R. Kirby, R. G. Sabat, J.-M. Nunzi, and O. Lebel, "Disperse and disordered: A mexylaminotriazine-substituted azobenzene derivative with superior glass and surface relief grating formation," *Journal of Materials Chemistry C: Materials for Optical and Electronic Devices*, vol. 2, no. 5, pp. 841–847, 2014.

[45] R. G. Sabat, "Superimposed surface-relief diffraction grating holographic lenses on azo-polymer films," *Optics Express*, vol. 21, no. 7, p. 8711, Apr. 2013.

[46] "PeakForce Tapping," Bruker, Tech. Rep.

[47] E. Dawson, "Inscription of Large Aperture Circular Gratings and the Surface Plasmon Resonance Response in the Optical Regime," Master's thesis, Royal Military College of Canada, Mar. 2024.

Appendix

Appendix A: Discrete MSPG Fabrication Parameters

Table A.1 – Target fabrication parameters for the discrete method, sextuple to decuple ($N = 6$ to $N = 10$) MSPGs. All gratings were inscribed at a constant irradiance of $I = 300\,\mathrm{mW/cm^2}$.

N	Grating	$\lambda_{\mathrm{target}}$ (nm)	$\Delta\lambda$ (nm)	Λ (nm)	T (s)
6	G1	650	40	414	200
	G2	690		440	60
	G3	730		465	60
	G4	770		490	60
	G5	810		516	60
	G6	850		541	60
7	G1	650	30	414	200
	G2	680		433	60
	G3	710		452	60
	G4	740		471	60
	G5	770		490	60
	G6	800		509	60
	G7	830		529	60
8	G1	650	30	414	200
	G2	680		433	60
	G3	710		452	60
	G4	740		471	60
	G5	770		490	60
	G6	800		509	60
	G7	830		529	60
	G8	860		548	60
9	G1	620	30	395	200
	G2	650		414	60
	G3	680		433	60
	G4	710		452	60
	G5	740		471	60
	G6	770		490	60
	G7	800		509	60
	G8	830		529	60
	G9	860		548	60
10	G1	590	30	376	200
	G2	620		395	60
	G3	650		414	60
	G4	680		433	60
	G5	710		452	60
	G6	740		471	60
	G7	770		490	60
	G8	800		509	60
	G9	830		529	60
	G10	860		548	60

Appendix B: Continuous MSPG Fabrication Parameters

Table B.1 – Target fabrication parameters for the gcontinuous method, sextuple to decuple ($N = 6$ to $N = 10$) MSPGs. All gratings were inscribed at a constant irradiance of $I = 300\,\mathrm{mW/cm^2}$.

N	Grating	$\lambda_{\mathrm{target}}$ (nm)	$\Delta\lambda$ (nm)	Λ (nm)	T (s)
6	G1	650	5	414	200
	G2	655		417	60
	G3	660		420	60
	G4	665		424	60
	G5	670		427	60
	G6	675		430	60
7	G1	650	5	414	200
	G2	655		417	60
	G3	660		420	60
	G4	665		424	60
	G5	670		427	60
	G6	675		430	60
	G7	680		433	60
8	G1	650	5	414	200
	G2	655		417	60
	G3	660		420	60
	G4	665		424	60
	G5	670		427	60
	G6	675		430	60
	G7	680		433	60
	G8	685		436	60
9	G1	650	5	414	200
	G2	655		417	60
	G3	660		420	60
	G4	665		424	60
	G5	670		427	60
	G6	675		430	60
	G7	680		433	60
	G8	685		436	60
	G9	690		439	60
10	G1	650	5	414	200
	G2	655		417	60
	G3	660		420	60
	G4	665		424	60
	G5	670		427	60
	G6	675		430	60
	G7	680		433	60
	G8	685		436	60
	G9	690		439	60
	G10	695		443	60

Appendix C: Spectral Validation Data

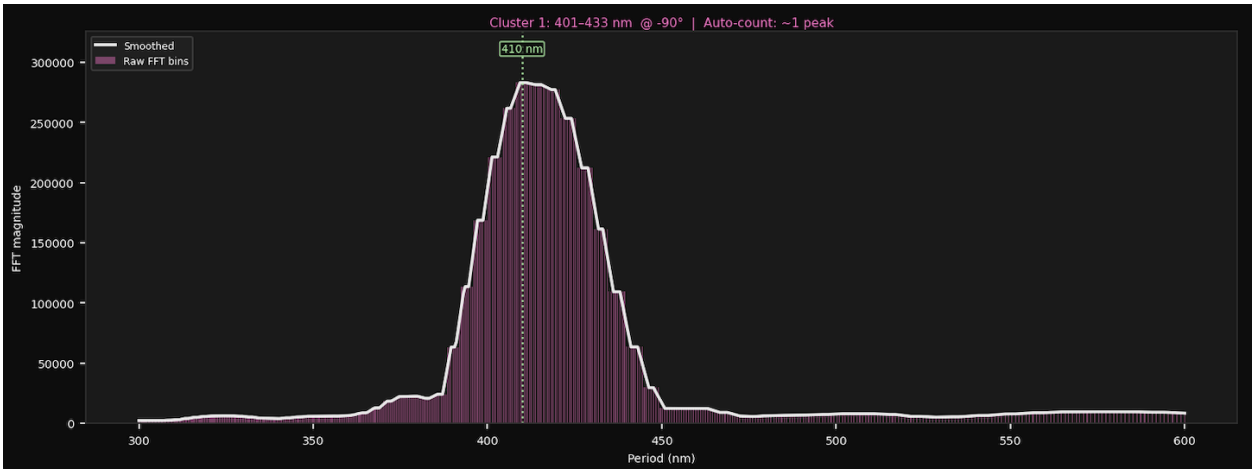

Figure C.1 – FFT analysis of a single grating ($N = 1$) as a baseline reference.

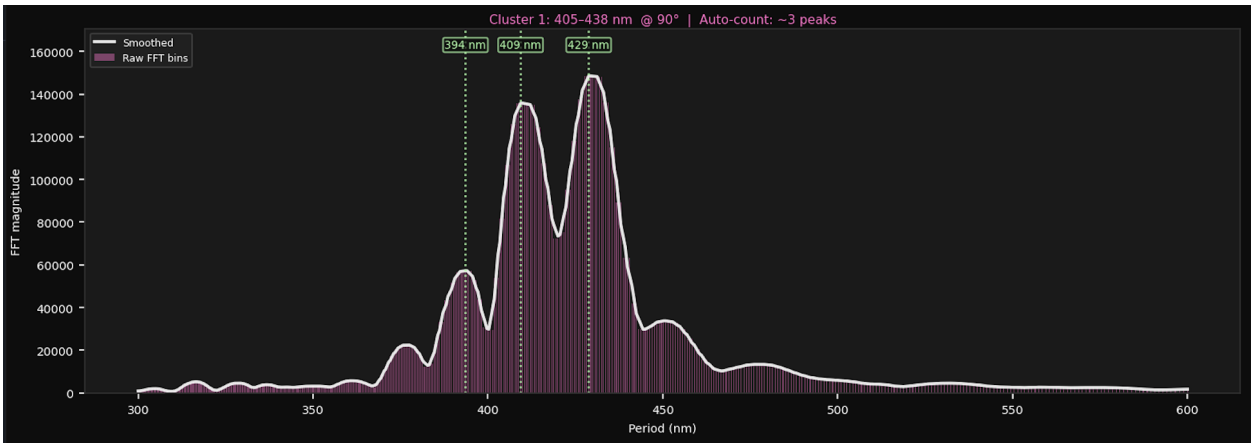

Figure C.2 – FFT analysis of a bi MSPG ($N = 2$).

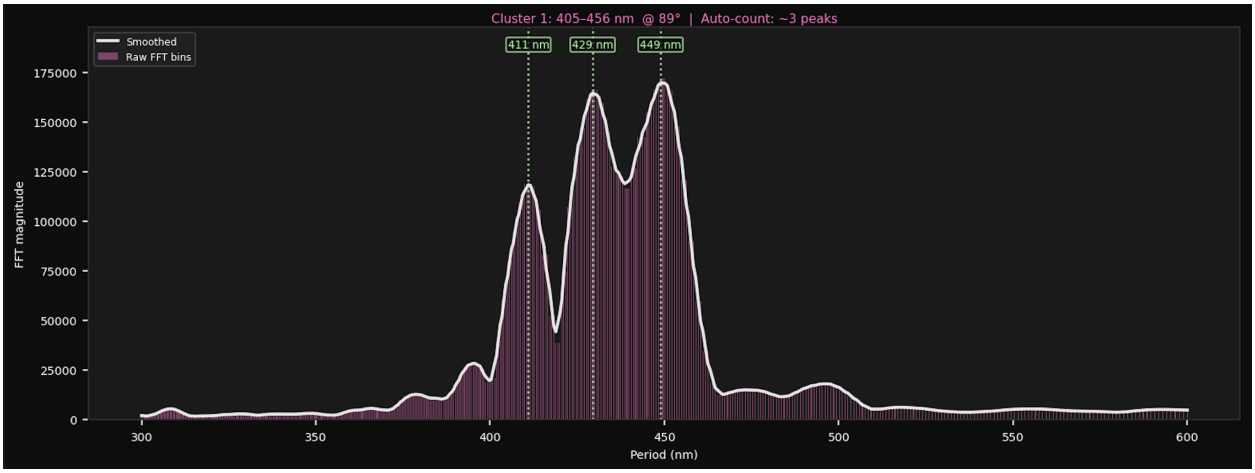

Figure C.3 – FFT analysis of a triple MSPG ($N = 3$).

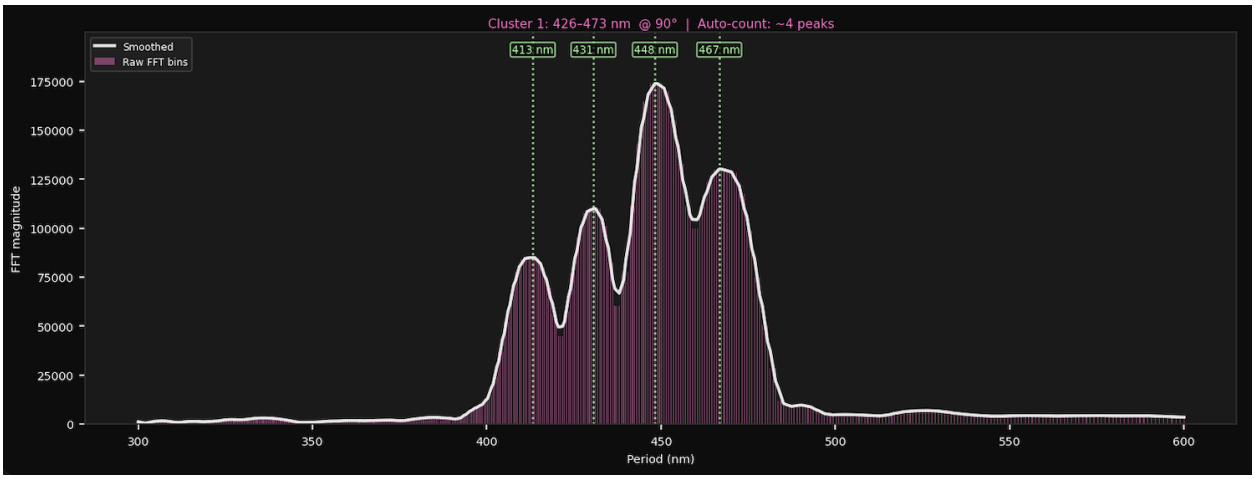

Figure C.4 – FFT analysis of a quadruple MSPG ($N = 4$).

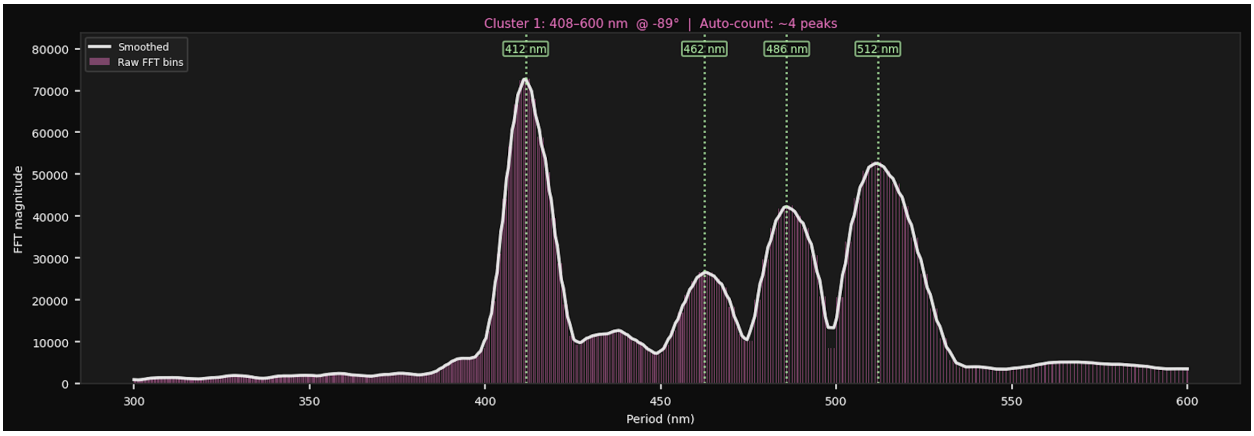

Figure C.5 – FFT analysis of a quintuple MSPG ($N = 5$).

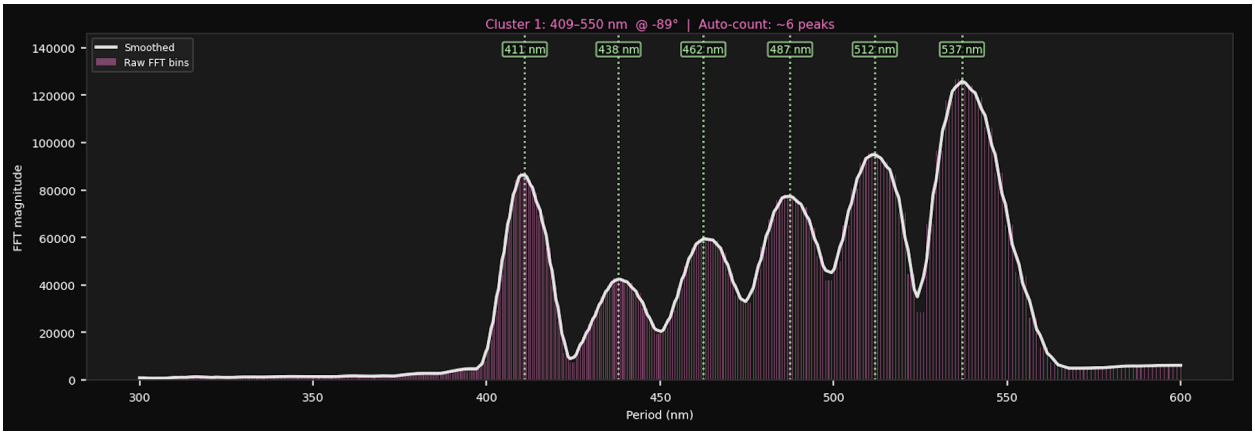

Figure C.6 – FFT analysis of a sextuple MSPG ($N = 6$).

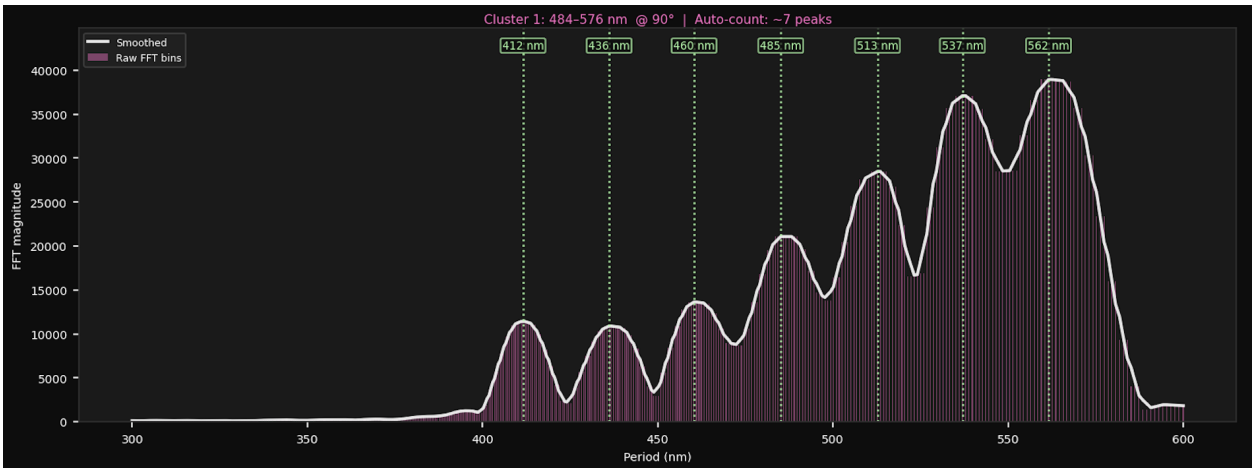

Figure C.7 – FFT analysis of a septuple MSPG ($N = 7$).

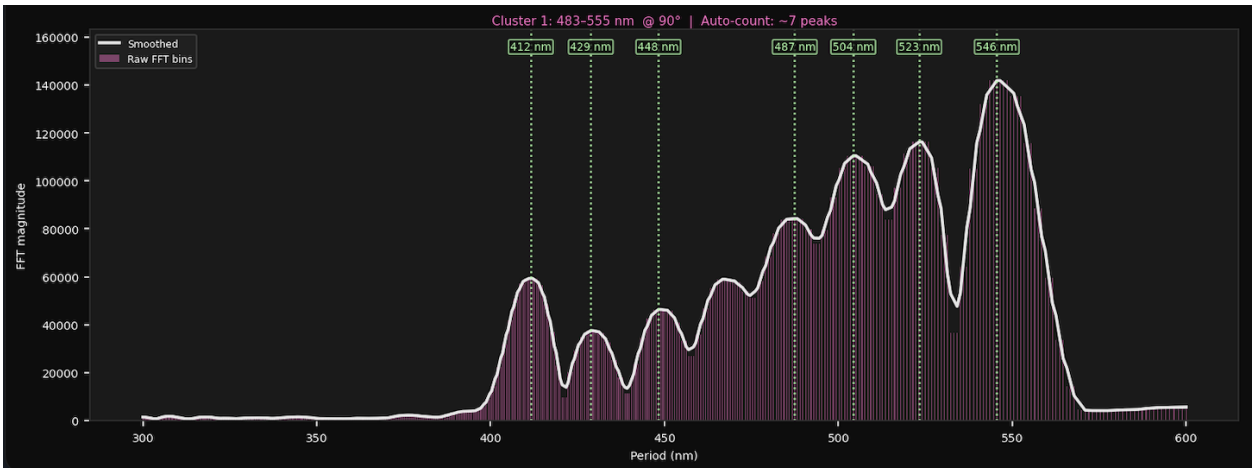

Figure C.8 – FFT analysis of an octuple MSPG ($N = 8$).

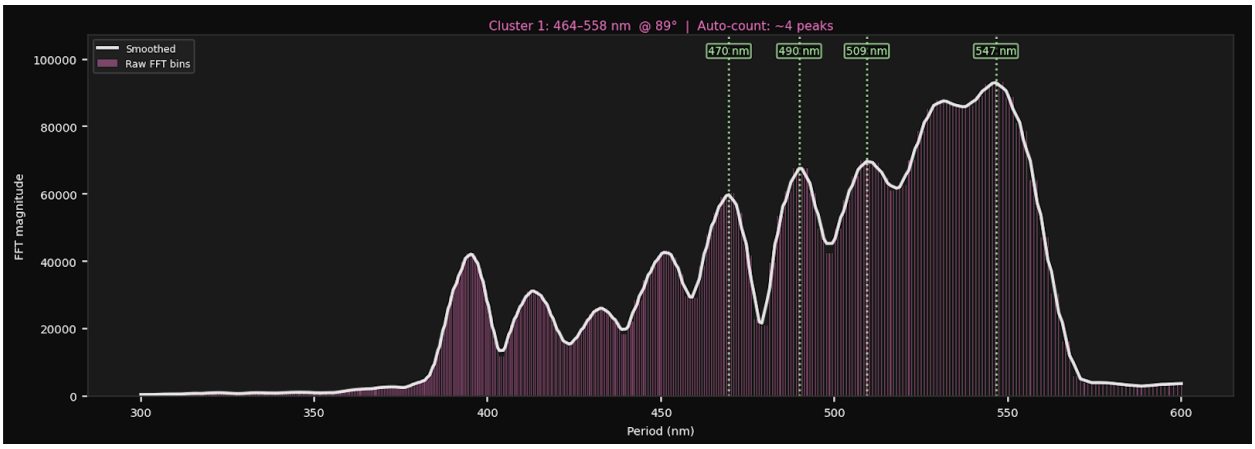

Figure C.9 – FFT analysis of a nonuple MSPG ($N = 9$).

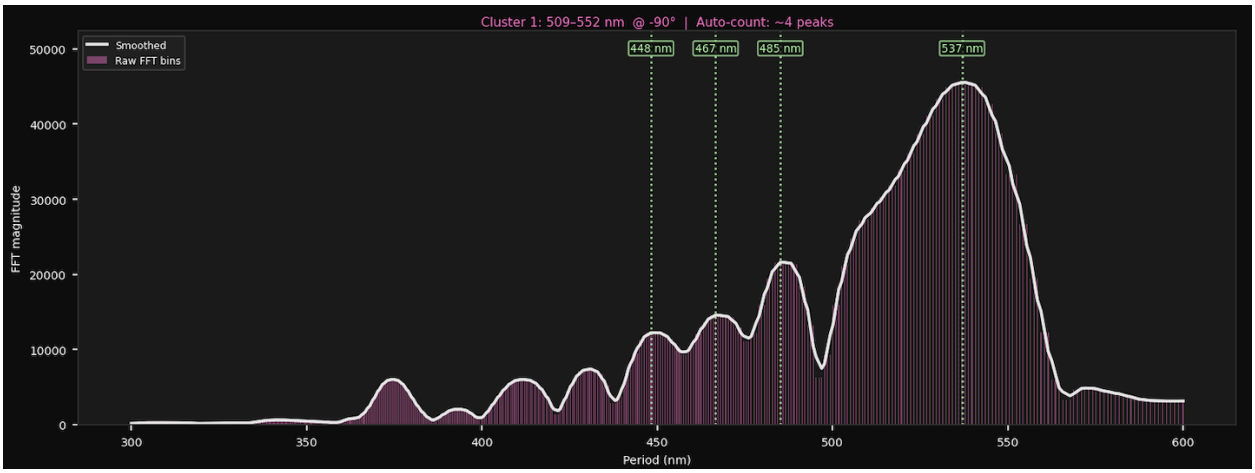

Figure C.10 – FFT analysis of a decuple MSPG ($N = 10$).

Note that for the highest order MSPGs ($N = 9$ and $N = 10$), the FFT analysis was less effective at uniquely identifying all individual periodicities. This is likely due to overlapping of closely spaced spatial frequency components which became indistinguishable from one another, as well as reaching the resolution limits of the FFT probability algorithm as constrained by the AFM scan resolution. As a result, some peaks appear to be broadened and merged, thus preventing clear resolution of each designed grating pitch.